

The High Temperature Superconductivity in Cuprates

PAOLO CEA^{(1)(2)(*)}

⁽¹⁾ *Dipartimento di Fisica dell'Università di Bari, I-70126 Bari, Italy*

⁽²⁾ *INFN - Sezione di Bari, I-70126 Bari, Italy*

Summary. — We discuss the high-temperature superconductivity in copper oxide ceramics. We propose an effective Hamiltonian to describe the dynamics of electrons or holes injected into the copper oxide layers. We show that our approach is able to account for both the pseudogap and the superconductivity gap. For the hole-doped cuprates we discuss in details the underdoped, optimal doped, and overdoped regions of the phase diagram. In the underdoped region we determine the doping dependence of the upper critical magnetic field, the vortex region, and the discrete states bounded to the core of isolated vortices. We explain the origin of the Fermi arcs and Fermi pockets. Moreover, we discuss the recently reported peculiar dependence of the specific heat on the applied magnetic field. We determine the critical doping where the pseudogap vanishes. We find that in the overdoped region the superconducting transition is described by the conventional d-wave BCS theory. We discuss the optimal doping region and the crossover between the underdoped region and the overdoped region. We also discuss briefly the electron-doped cuprate superconductors.

PACS 74.20.-z, 74.72.-h, 74.72.Gh, 74.72.Ek - .

1. – Introduction

Since the discovery of superconductivity in the copper oxide ceramics (cuprates) [1], both theoretical and experimental efforts have been made to investigate the physical mechanism responsible for superconductivity with an unprecedented high transition temperature T_c (for recent reviews see Refs. [2, 3, 4, 5, 6, 7, 8, 9]). Despite this, an understanding of the superconducting pairing of the high-temperature superconductors is still lacking.

Very soon after the discovery of the high temperature superconductors, it was realized [10] that superconductivity were intimately related to the square planar CuO_2 lattice. Moreover, the physics of the CuO_2 planes were well described by the nearly half-filled Hubbard model with moderately on-site Coulomb repulsion.

(*) Paolo.Cea@ba.infn.it

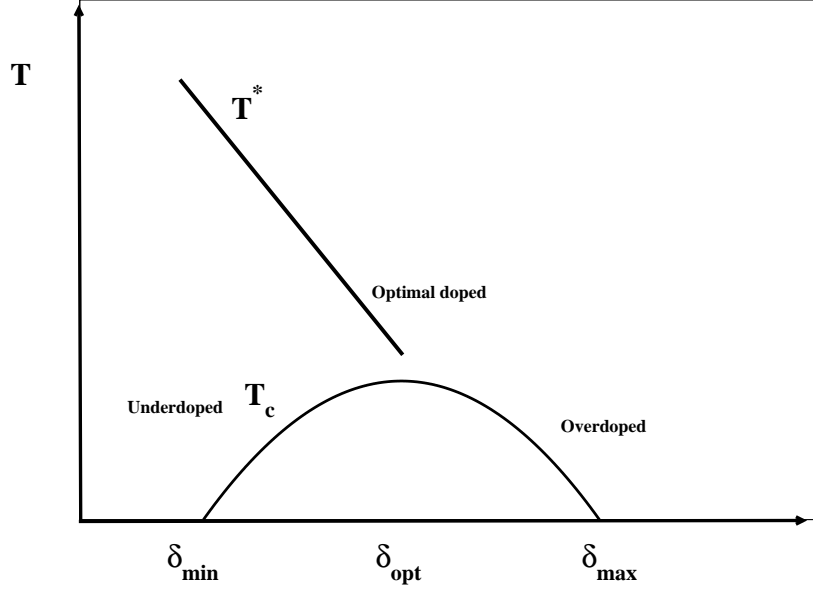


Fig. 1. – Schematic phase diagram of hole-doped cuprate high-temperature superconductors. Carrier concentrations δ near to the maximum critical temperature $T_c(\delta_{opt})$ locate the optimal doped region. Regions with lower and larger hole concentration are called underdoped and overdoped, respectively. The temperature T^* is the pseudogap temperature.

The microscopic model for the description of electrons in the CuO_2 layers is believed to be the effective single-band Hubbard model: ⁽¹⁾

$$(1.1) \quad \hat{H} = -t \sum_{\langle i,j \rangle, \sigma} \left[\hat{c}_{i,\sigma}^\dagger \hat{c}_{j,\sigma} + \hat{c}_{j,\sigma}^\dagger \hat{c}_{i,\sigma} \right] + U \sum_i \hat{n}_{i,\uparrow} \hat{n}_{i,\downarrow}, \quad \hat{n}_{i,\sigma} = \hat{c}_{i,\sigma}^\dagger \hat{c}_{i,\sigma},$$

where $\hat{c}_{i,\sigma}^\dagger$ and $\hat{c}_{i,\sigma}$ are creation and annihilation operators for electrons with spin σ , U is the onsite Coulomb repulsion for electrons of opposite spin at the same atomic orbital, and t is the hopping parameter. As is well known [12], the superexchange mechanism yields a Heisenberg antiferromagnetic exchange interaction with $J = \frac{4t^2}{U}$ between spins on the Cu atoms. Since $U \gg t$, at half-filling the onsite Coulomb repulsion gives an insulator where the electron spins are antiferromagnetically ordered.

The phase diagram resulting from tuning the doping of CuO_2 planes with holes is shown schematically in Fig. 1. At half-filling, corresponding to $\delta = 0$, we have a Mott insulator with long range antiferromagnetic order which disappears for temperatures above the critical Néel temperature T_N (not shown in Fig. 1). By adding holes into the CuO_2 planes ($\delta > 0$) the long range antiferromagnetic order is rapidly destroyed. Superconductivity occurs beyond a minimal hole content $\delta_{min} \simeq 0.05 - 0.06$ where there is no long-range antiferromagnetic order. Nevertheless, signs of magnetism persist [13] in the hole-doped materials with $\delta > \delta_{min}$ as local order on a short length scale $\xi_{AF} \gtrsim 10^{-6} cm$, as observed

⁽¹⁾ For a lucid discussion see Ref. [11].

in muon spin relaxation [14] and neutron scattering [15, 16, 17] measurements.

The superconducting critical temperature T_c rises with increasing hole doping through the underdoped region ($\delta < \delta_{opt}$), reaches a peak at optimal doping $\delta \simeq \delta_{opt}$, falls away at higher doping $\delta > \delta_{opt}$ (overdoped region), and then vanishes at the maximal doping $\delta_{max} \simeq 0.3$. This peculiar doping dependence of the critical temperature T_c is a generic feature of the hole-doped copper oxides. Another generic feature of the high-temperature cuprate superconductors is the presence of a pseudogap $k_B T^*$ (k_B being the Boltzmann's constant) in the underdoped region $\delta \lesssim \delta_{opt}$. The pseudogap was first detected in the temperature dependence of the spin-lattice relaxation, Knight shift, and magnetic susceptibility studies ⁽²⁾. The pseudogap temperature T^* is much larger than the superconducting critical temperature T_c in the underdoped region. Moreover, $T^*(\delta)$ decreases upon increasing the doping and seems to merge with $T_c(\delta)$ for $\delta \simeq \delta_{opt}$. In the overdoped region, however, the coexistence of the superconducting gap with the pseudogap is still subject to an intense debate.

The challenge is to find a theory that is rooted in the microscopic physics of the copper oxides which is able to account for the physics of the pseudogap and the superconductivity. One of the problem in constructing a satisfactory microscopic theory of the high-temperature superconductivity is to isolate that part of the interaction which is responsible for both the pseudogap and the superconductivity in cuprates. The purpose of this paper is to present an approach which, according to the spirit of the conventional superconductivity theory of Bardeen, Cooper, and Schrieffer [18] (BCS), allows to isolate an effective Hamiltonian governing the dynamics of the electrons or holes injected into the undoped copper-oxide planes. We shall assume that the superconductivity originates into the CuO_2 planes, and thereby we shall neglect the motion along the direction perpendicular to the planes. We further assume that electron dynamics in the CuO_2 planes is described by the single-band effective Hubbard model with Hamiltonian given by Eq. (1.1). Since the majority of high-temperature cuprate superconductors are hole-doped, we shall focus mainly on hole-doped cuprates. Nevertheless, in Section 6 we briefly discuss also the electron-doped cuprates (for a recent review, see Ref. [19]).

The plan of the paper is as follows. In Sect. 2 we set up the effective interaction between two holes in an antiferromagnetic background and we discuss the main assumptions of the paper. Section 3 is devoted to a general discussion of the physical structure of the superconducting ground state. In Sect. 3.1 we discuss the real-space d-wave bound states of two holes; in Sect. 3.2 we address the problem of the superconductivity and pseudogap in the underdoped region. In Sect. 3.3 we discuss the d-wave BCS ground state and argue that it is relevant in the overdoped region. In Sect. 3.4 we present our understanding of the phase diagram of hole-doped cuprates. The physics of the underdoped region is presented in Sect. 4 where we discuss the real-space bound states in an external magnetic field (Sect. 4.1), the upper critical magnetic field (Sect. 4.2), the vortex region (Sect. 4.3), the physics of Fermi arcs and quantum oscillations (Sect. 4.4). Section 5 is devoted to the discussion of the physics in the overdoped and optimal doped regions together with the crossover between the underdoped region and the overdoped region. In Sect. 6 we briefly address the problem of superconductivity and pseudogap in the electron-doped cuprates. Finally, in Section 7 we summarize the main achievements of the paper and we draw our conclusions.

⁽²⁾ See Ref. [8] and references therein.

2. – The effective Hamiltonian

In this Section we set up our effective Hamiltonian for the dynamics of holes in the nearly half-filled single-band Hubbard model. As discussed in the Introduction, we are assuming that the superconductivity in cuprates is related to the square planar CuO_2 lattice. The single-band Hamiltonian is given by Eq. (1.1), where $\langle i, j \rangle$ denotes a pair of nearest-neighbor sites of a square lattice with lattice constant a_0 (see Fig. 2). Let M be the number of sites of the copper lattice and N the number of electrons. In the half filled lattice $N = M$, i.e. there is exactly one electron per site. In the underfilled case $N < M$ there are holes with doping fraction (number of holes per site):

$$(2.1) \quad \delta = 1 - \frac{N}{M} .$$

In the subspace of the state space of avoided double occupancies of Cu sites, the one-band Hubbard model may be canonically transformed into the so-called $t - J$ Hamiltonian:

$$(2.2) \quad \hat{H} = -t \sum_{\langle i, j \rangle, \sigma} \left[\hat{C}_{i, \sigma}^\dagger \hat{C}_{j, \sigma} + \hat{C}_{j, \sigma}^\dagger \hat{C}_{i, \sigma} \right] + J \sum_{\langle i, j \rangle} \left[\vec{S}_i \cdot \vec{S}_j - \frac{1}{4} \hat{n}_i \hat{n}_j \right] ,$$

where

$$(2.3) \quad \hat{C}_{i, \sigma} = \hat{c}_{i, \sigma} (1 - \hat{n}_{i, -\sigma}) , \quad J = \frac{4t^2}{U} ,$$

and \vec{S}_i is the spin- $\frac{1}{2}$ operator at site i .⁽³⁾ Since at half-filling $\hat{n}_{i, -\sigma} = 1$, the $t - J$ Hamiltonian Eq. (2.2) reduces to the square lattice Heisenberg Hamiltonian:

$$(2.4) \quad \hat{H} = J \sum_{\langle i, j \rangle} \vec{S}_i \cdot \vec{S}_j .$$

The ground state of the latter Hamiltonian is known to be the antiferromagnetic Néel state. When the system is doped with holes away from half filling ($\delta > 0$), the dynamics is no longer described by the Heisenberg Hamiltonian Eq. (2.4), but one must use the $t - J$ Hamiltonian Eq. (2.2) with the supplementary constraint of no double occupied lattice sites. It is easy to see that the motion of dilute holes in the antiferromagnetic Néel background is strongly frustrate. Indeed, when a hole hops from one site to its nearest neighbor, a spin is also moved onto one lattice site with the wrong spin orientation with respect to the antiferromagnetic background. On the other hand, a pair of holes with nearest-neighbor distance (see Fig. 2) can move almost freely without destroying the antiferromagnetic background. The effective Hamiltonian for the propagation of the holes in the antiferromagnetic background can be written as [21, 22]:

$$(2.5) \quad \hat{H}_0 = -\frac{t^2}{U} \sum_{\vec{r}} \sum_{i, j} \hat{\psi}_h^\dagger(\vec{r} + \vec{i}a_0 + \vec{j}a_0) \hat{\psi}_h(\vec{r}) ,$$

⁽³⁾ See, for instance, Ref. [20] and references therein.

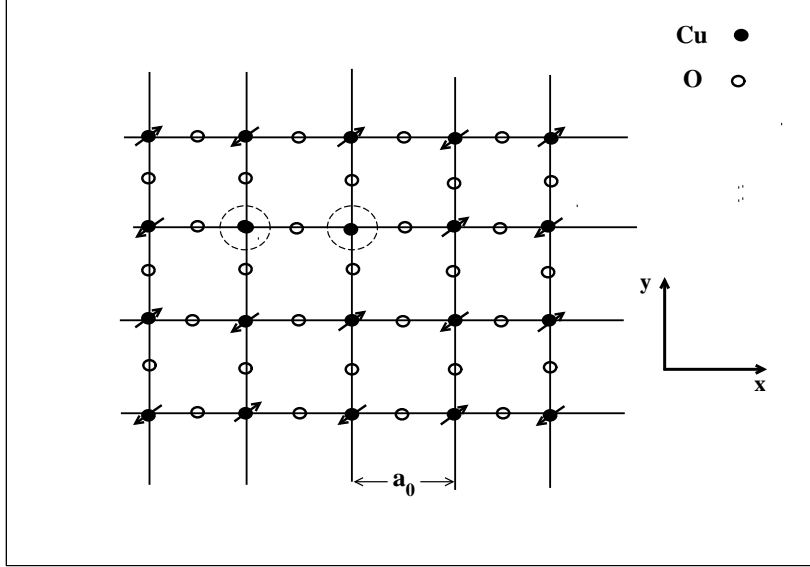


Fig. 2. – The idealized square copper plane with lattice spacing a_0 . The dashed ellipses represent two holes in an antiferromagnetic background.

where $\hat{\psi}_h^\dagger(\vec{r})$, $\hat{\psi}_h(\vec{r})$ are creation and annihilation operators for holes at the lattice site \vec{r} and the sum over the direction vectors \vec{i} and \vec{j} is restricted to next-nearest neighbor lattice sites. Note that in the effective Hamiltonian \hat{H}_0 we do not display the spin of the holes since the antiferromagnetic background forces the two holes to have antiparallel spins. In other words, the motion of a hole must not disturb the antiferromagnetic background. Moreover, in this antiferromagnetic background approximation, it turns out that there is an effective attractive two-body potential between nearest-neighbor holes [21]. However, it has been pointed out [23] that the motion of a pair of holes, which naively should be mobile, is frustrated due to fermionic nature of the background spins. Indeed, for states with two holes as nearest neighbors in an antiferromagnetic background it is easy to see [24] that there are configurations that differ by the exchange of two electrons. The destructive interference of these configurations leads to holes with very large effective mass. This problem can be avoided if we consider pairs of hole with distance much greater than the lattice spacing. Accordingly, we shall suppose that two holes with distance $a_0 \ll r_0 \ll \xi_{AF}$, where ξ_{AF} is the antiferromagnetic local order length scale, are subject to an effective attractive two-body potential. Our proposal is quite similar to the spin-bag theory [25] where the pairing is due to a local reduction of the antiferromagnetic order (bag) shared by two holes.

Thus, we are lead to consider the following reduced interaction Hamiltonian:

$$(2.6) \quad \hat{H}_{int} = \frac{1}{2} \int d\vec{r}_1 d\vec{r}_2 \hat{\psi}_{h,\uparrow}^\dagger(\vec{r}_1) \hat{\psi}_{h,\downarrow}^\dagger(\vec{r}_2) V(\vec{r}_1 - \vec{r}_2) \hat{\psi}_{h,\downarrow}(\vec{r}_2) \hat{\psi}_{h,\uparrow}(\vec{r}_1).$$

The simplest choice for the two-body potential $V(\vec{r}_1 - \vec{r}_2)$ is:

$$(2.7) \quad V(\vec{r}_1 - \vec{r}_2) = \begin{cases} \infty & \vec{r}_1 = \vec{r}_2 \\ -V_0 & |\vec{r}_1 - \vec{r}_2| \leq r_0(\delta) \\ 0 & \text{otherwise} \end{cases}$$

where the hard-core at the origin is imposed to avoid configurations where two holes are on the same site. Moreover, since we are considering the limit of low carriers, $\delta \ll 1$, the hard-core potential does not allow two holes to come too close, thereby implementing the no-double occupation constraint. As concern the range of our potential $r_0(\delta)$, it is natural to choice $r_0(\delta)$ of the order of the coherence length $\xi_0 \simeq 6a_0$. So that we assume:

$$(2.8) \quad r_0(\delta) = 6 a_0 \left(1 - \frac{\delta}{\delta_c}\right)^{\frac{1}{2}}, \quad \delta_c \simeq 0.35.$$

The peculiar dependence on the doping fraction δ arises as follows. The attractive two-body potential originates from the interaction of two holes in the antiferromagnetic background which extends over a distance of order ξ_{AF} . Since the injected holes tend to destruct the antiferromagnetic order, the area of the antiferromagnetic islands should decrease with increasing δ . In addition, as discussed in the Introduction (see Fig. 1), the superconducting instability disappears at the maximal doping $\delta_{max} \simeq 0.30$. The simplest parameterization which takes care of these effects leads to our Eq. (2.8). Regarding the parameter V_0 in Eq. (2.7), we have fixed this parameter such that there is at least one real space d-wave bound state. To this end it suffices to assume:

$$(2.9) \quad V_0 \simeq 2J = \frac{8t^2}{U}.$$

In the following we will use the numerical values:

$$(2.10) \quad a_0 \simeq 4.0 \cdot 10^{-8} \text{ cm}, \quad t \simeq 0.11 \text{ eV}, \quad U \simeq 1.1 \text{ eV},$$

that are appropriate for a typical cuprate. Note that the resulting Néel temperature:

$$(2.11) \quad T_N \simeq \frac{J}{k_B} \sim 10^3 \text{ K}$$

is of the order of the observed Néel temperatures in cuprates.

Before concluding this Section, we would like to rewrite the Hamiltonian \hat{H}_0 Eq. (2.5) in the limit of low-lying excitations. Observing that \hat{H}_0 can be diagonalized by writing:

$$(2.12) \quad \hat{\psi}_h(\vec{r}) = \frac{1}{\sqrt{M}} \sum_{\vec{k}} \exp(i\vec{k} \cdot \vec{r}) \hat{\psi}_h(\vec{k}),$$

so that:

$$(2.13) \quad \hat{\psi}_h(\vec{k}) = \frac{1}{\sqrt{M}} \sum_{\vec{r}} \exp(-i\vec{k} \cdot \vec{r}) \hat{\psi}_h(\vec{r}).$$

We get:

$$(2.14) \quad \hat{H}_0 = \sum_{\vec{k}} \varepsilon_{\vec{k}} \hat{\psi}_h^\dagger(\vec{k}) \hat{\psi}_h(\vec{k}) ,$$

where:

$$(2.15) \quad \varepsilon_{\vec{k}} = - \frac{2t^2}{U} [\cos(2k_x a_0) + \cos(2k_y a_0)] .$$

We now take the small-k limit:

$$(2.16) \quad \hat{H}_0 = \sum_{\vec{k}} \frac{\hbar^2 \vec{k}^2}{2 m_h^*} \hat{\psi}_h^\dagger(\vec{k}) \hat{\psi}_h(\vec{k})$$

with:

$$(2.17) \quad m_h^* = \frac{\hbar^2}{8 \frac{t^2}{U} a_0^2} .$$

So that we may write for the effective Hamiltonian:

$$(2.18) \quad \hat{H}_0 = \sum_{\sigma=\uparrow,\downarrow} \int d\vec{r} \hat{\psi}_{h,\sigma}^\dagger(\vec{r}) \left(\frac{-\hbar^2 \nabla^2}{2 m_h^*} \right) \hat{\psi}_{h,\sigma}(\vec{r}) ,$$

where we make explicit the spin degrees of freedom. Using the numerical values of the parameters we obtain:

$$(2.19) \quad m_h^* \simeq 5.41 m_e ,$$

where m_e is the electron mass. To summarize, our effective Hamiltonian for low-lying excitations may be described by:

$$(2.20) \quad \hat{H}_{eff} = \hat{H}_0 + \hat{H}_{int} ,$$

with \hat{H}_0 and \hat{H}_{int} given by Eqs. (2.18) and (2.6) respectively. It is worthwhile to stress that the arguments developed in this Section cannot be considered as a truly microscopic derivation of the effective Hamiltonian Eq. (2.20).

3. – The superconducting ground state

For later convenience it is useful to think about the wave function of the superconducting ground state within the BCS theory. Let $\varphi(\vec{r}_1 - \vec{r}_2)$ be the wavefunction of a Cooper pair [26], thus the superconducting ground state may be expressed as an antisymmetrized product of identical pair functions:

$$(3.1) \quad \Omega(\vec{r}_1, \dots, \vec{r}_N) = \sum_P (-1)^P P \{ \varphi(\vec{r}_1 - \vec{r}_2) \cdots \varphi(\vec{r}_{N-1} - \vec{r}_N) \} ,$$

in which the sum is over all permutations P of the N particles. The expression Eq. (3.1) may be used to point out the analogies and differences between the superconducting ground state and that of a Bose-Einstein condensation of pairs [27, 28]. Indeed, a Bose-Einstein condensate of pairs would also be given as a product of identical pair wavefunctions. The process of antisymmetrizing would not change the character of the state very much if the size of the pair wavefunction, ξ_0 , were small compared with the average spacing between pairs. In this case, wavefunctions in the sum differing by the exchange of single members of two or more pairs would not overlap very much, and the system would behave qualitatively like a condensed Bose-Einstein gas. However, antisymmetrization makes a major difference if the size of the pair wavefunction is large compared with the spacing between pairs. In this case, it is convenient to rewrite the superconducting ground-state wavefunction Eq. (3.1) in the second quantization formalism. To this end, we introduce the creation operator of a pair at rest:

$$(3.2) \quad b^\dagger = \int d\vec{r}_1 d\vec{r}_2 \varphi(\vec{r}_1 - \vec{r}_2) \hat{\psi}_\uparrow^\dagger(\vec{r}_1) \hat{\psi}_\downarrow^\dagger(\vec{r}_2).$$

Then, the wavefunction Eq. (3.1) can be written as:

$$(3.3) \quad |\Omega\rangle_N = \frac{(b^\dagger)^{N'}}{N'!} |0\rangle,$$

where $|0\rangle$ is the vacuum, and $N' = \frac{N}{2}$ is the number of pairs. Now, from the identity [29]:

$$(3.4) \quad |\Omega\rangle_N = \frac{1}{2\pi} \int_0^{2\pi} d\phi e^{-iN'\phi} \exp[e^{i\phi} b^\dagger] |0\rangle,$$

we argue that the state:

$$(3.5) \quad |\Omega\rangle_{BCS} = \exp[e^{i\phi} b^\dagger] |0\rangle$$

is the superconducting ground state for a system with varying number of particles. Obviously, in that case the relevant Hamiltonian is $\hat{H} - \mu\hat{N}$, where μ is the chemical potential. From Eq. (3.2) we obtain:

$$(3.6) \quad b^\dagger = \sum_{\vec{q}} \varphi(\vec{q}) \hat{c}_{\vec{q},\uparrow}^\dagger \hat{c}_{-\vec{q},\downarrow}^\dagger,$$

where:

$$(3.7) \quad \varphi(\vec{r}_1 - \vec{r}_2) = \sum_{\vec{q}} \exp[i\vec{q} \cdot (\vec{r}_1 - \vec{r}_2)] \varphi(\vec{q}).$$

Using Eq. (3.6) it is easy to find:

$$(3.8) \quad |\Omega\rangle_{BCS} = \prod_{\vec{q}} \mathcal{N}_{\vec{q}} \left[1 + e^{i\phi} \varphi(\vec{q}) \hat{c}_{\vec{q},\uparrow}^\dagger \hat{c}_{-\vec{q},\downarrow}^\dagger \right] |0\rangle,$$

with the normalization factor $\mathcal{N}_{\vec{q}}$. Indeed, Eq. (3.8) agrees with the well-known BCS variational ground state:

$$(3.9) \quad |O\rangle_{BCS} = \prod_{\vec{q}} \left[u(\vec{q}) + v(\vec{q}) \hat{c}_{\vec{q},\uparrow}^\dagger \hat{c}_{-\vec{q},\downarrow}^- \right] |0\rangle ,$$

with the normalization:

$$(3.10) \quad |u(\vec{q})|^2 + |v(\vec{q})|^2 = 1 .$$

As we discuss later on, the superconducting ground-state wave function in the form of Eq. (3.1) will be of relevance in the underdoped region, while in the overdoped region the BCS variational ground state Eq. (3.9) would be more appropriate.

3.1. Real space *d*-wave bound states. – We are interested in the problem of two holes in interaction with the effective two-body potential Eq. (2.7). The resulting Schrödinger equation is:

$$(3.11) \quad \left[-\frac{\hbar^2}{2m_h^*} (\nabla_{\vec{r}_1}^2 + \nabla_{\vec{r}_2}^2) + V(\vec{r}_1 - \vec{r}_2) \right] \Phi(\vec{r}_1 - \vec{r}_2) = E \Phi(\vec{r}_1 - \vec{r}_2) .$$

According to the reduced interaction Hamiltonian Eq. (2.6) the holes have antiparallel spins, so that the wavefunction $\Phi(\vec{r}_1 - \vec{r}_2)$ must be symmetric under hole interchange. Introducing:

$$(3.12) \quad \vec{r} = \vec{r}_1 - \vec{r}_2 \quad , \quad \vec{R} = \frac{\vec{r}_1 + \vec{r}_2}{2} ,$$

we rewrite Eq. (3.11) as:

$$(3.13) \quad \left[-\frac{\hbar^2}{2m_h^*} \left(2\nabla_{\vec{r}}^2 + \frac{1}{2}\nabla_{\vec{R}}^2 \right) + V(r) \right] \Phi(\vec{R}, \vec{r}) = E \Phi(\vec{R}, \vec{r}) ,$$

whereupon:

$$(3.14) \quad \Phi(\vec{R}, \vec{r}) = \exp(i\vec{K} \cdot \vec{R}) \varphi(\vec{r}) ,$$

$$(3.15) \quad E = \frac{\hbar^2 \vec{K}^2}{4m_h^*} - \Delta ,$$

$$(3.16) \quad \left[-\frac{\hbar^2}{m_h^*} \nabla_{\vec{r}}^2 + V(r) \right] \varphi(\vec{r}) = -\Delta \varphi(\vec{r}) .$$

Without loss in generality, we may assume that the center of mass of the pair is at rest, $\vec{P} = \hbar \vec{K} = 0$. Since the potential is central we may adopt polar coordinates. We have:

$$(3.17) \quad \varphi(r, \theta) = \frac{\exp(im\theta)}{\sqrt{2\pi}} \varphi_m(r) ,$$

Inserting into Eq. (3.16) and using Eq. (2.7) we get:

$$(3.18) \quad \varphi_m(r=0) = 0 ,$$

$$(3.19) \quad \left[\frac{d^2}{dr^2} + \frac{1}{r} \frac{d}{dr} - \frac{m^2}{r^2} + \frac{m_h^*}{\hbar^2} (-\Delta_m + V_0) \right] \varphi_m(r) = 0 , \quad 0 < r < r_0(\delta) ,$$

$$(3.20) \quad \left[\frac{d^2}{dr^2} + \frac{1}{r} \frac{d}{dr} - \frac{m^2}{r^2} - \frac{m_h^*}{\hbar^2} \Delta_m \right] \varphi_m(r) = 0 , \quad r_0(\delta) < r .$$

Since $\varphi_m(r)$ is even and must satisfy Eq. (3.18), we have $m = 2, 4, \dots$. With our choice of the parameters, Eqs. (2.8), (2.9) and (2.10), it is straightforward to check that there are bound states ($\Delta_m > 0$) only for $m = 2$ (d-wave). In this case we get:

$$(3.21) \quad \varphi_2(r) = \begin{cases} A J_2(\tilde{k}r) & r < r_0(\delta) \\ B K_2(\tilde{\kappa}r) & r_0(\delta) < r \end{cases}$$

where $J_2(x)$ and $K_2(x)$ are Bessel functions,

$$(3.22) \quad \tilde{\kappa}^2 = \frac{m_h^*}{\hbar^2} \Delta_2 , \quad \tilde{k}^2 = \frac{m_h^*}{\hbar^2} (V_0 - \Delta_2) ,$$

and

$$(3.23) \quad \tilde{\kappa}r_0(\delta) \frac{K_2'(\tilde{\kappa}r_0(\delta))}{K_2(\tilde{\kappa}r_0(\delta))} = \tilde{k}r_0(\delta) \frac{J_2'(\tilde{k}r_0(\delta))}{J_2(\tilde{k}r_0(\delta))} .$$

With the further definitions:

$$(3.24) \quad x_0 = \tilde{k}_0 r_0(\delta) , \quad \tilde{k}_0^2 = \frac{m_h^* V_0}{\hbar^2} , \quad \zeta = \frac{\tilde{k}}{\tilde{k}_0} ,$$

one can rewrite Eq. (3.23) as:

$$(3.25) \quad x_0 \sqrt{1 - \zeta^2} \frac{K_2'(x_0 \sqrt{1 - \zeta^2})}{K_2(x_0 \sqrt{1 - \zeta^2})} = x_0 \zeta \frac{J_2'(x_0 \zeta)}{J_2(x_0 \zeta)} .$$

It is not too hard to see that Eq. (3.25) allows non trivial solutions if the *effective* wall-depth x_0 satisfies:

$$(3.26) \quad x_0 \geq \bar{x}_0 , \quad \bar{x}_0 \simeq 3.8317 ,$$

where \bar{x}_0 is the solution of:

$$(3.27) \quad x \frac{J_2'(x)}{J_2(x)} + 2 = 0 .$$

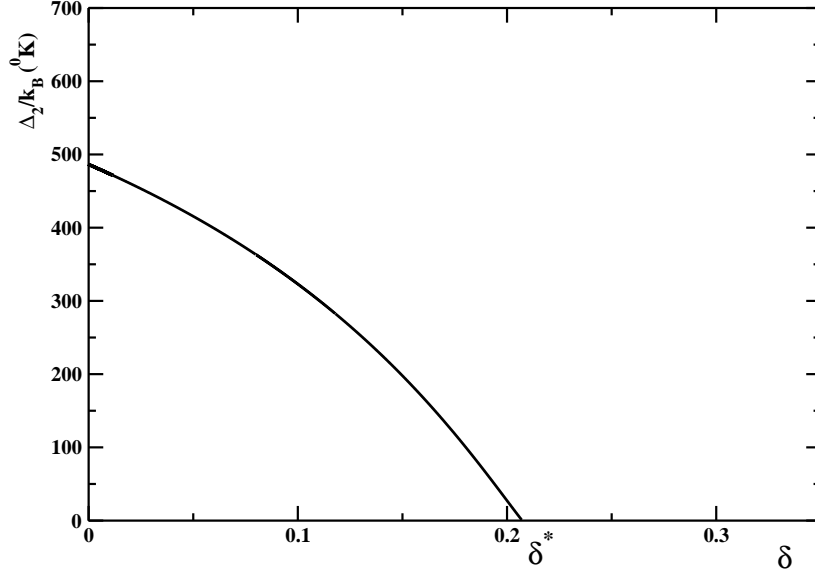


Fig. 3. – The gap $\Delta_2(\delta)$ versus the hole doping fraction δ . According to Eq. (3.28) $\delta^* \simeq 0.207$.

From Eq (3.26) it follows that there are non trivial solutions for hole doping such that:

$$(3.28) \quad 0 \leq \delta \leq \delta^* \quad , \quad \delta^* \simeq 0.207 .$$

In fact, in Fig 3 we display $\Delta_2(\delta)$ versus the hole doping fraction δ . We see that the gap $\Delta_2(\delta)$ decreases rapidly with δ and vanishes at $\delta = \delta^*$ according to Eq. (3.28). Note that, with our parameters, we have $\Delta(0) \simeq 486 K \cdot k_B$ which should be compared with $V_0 \simeq 1021 K \cdot k_B$. From Figure 4, where we display the normalized wavefunction $\varphi_2(r)$, Eq. (3.21), for a typical value of δ , we see that our bound-state wavefunction extends up to distance $r \sim 6a_0$.

Since the eigenvalue equations Eqs. (3.19) and (3.20) depend on m^2 , the general d-wave wavefunction is a linear combination of $\varphi_2(r)$ and $\varphi_{-2}(r)$. From the geometry of the CuO_2 planes we are lead to assume:

$$(3.29) \quad \varphi_2(r, \theta) = \varphi_2(r) \cdot \cos(2\theta) ,$$

where the coordinate axis are directed along the $Cu-O$ bond directions as in Fig. 2. This is the most natural choice since the wavefunction is sizable along the $Cu-O$ bonds and vanishes at $\theta = \pm \frac{\pi}{4}$. For later convenience, we need to evaluate the Fourier transform of the wavefunction Eq. (3.29). We have:

$$(3.30) \quad \tilde{\varphi}_2(\vec{k}) = \int d\vec{r} \varphi_2(r, \theta) \exp(i\vec{k} \cdot \vec{r}) .$$

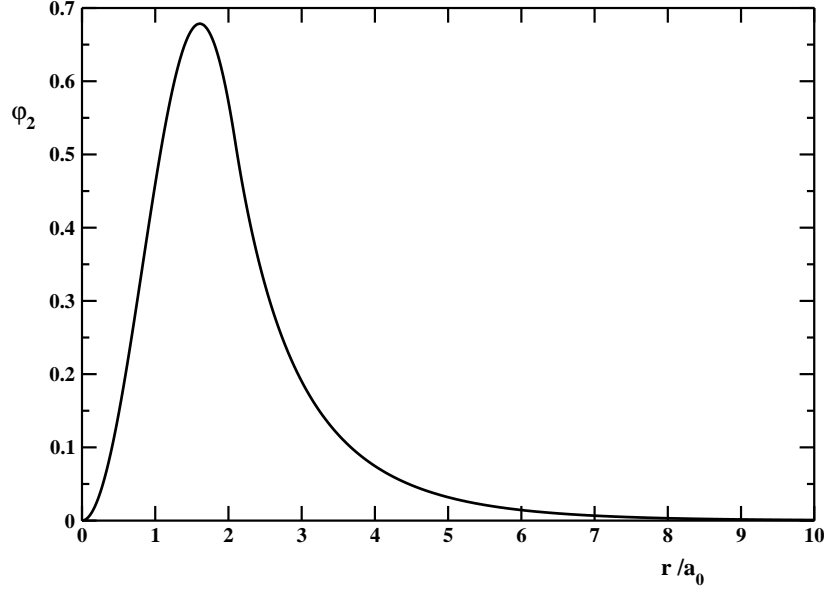


Fig. 4. – The normalized d-wave wavefunction φ_2 for $\delta = 0.18$.

Assuming that the k_x, k_y axis are oriented along the copper-oxygen bond directions, and using the expansion:

$$(3.31) \quad \exp(i\vec{k} \cdot \vec{r}) = \exp(ikr \cos \theta_{kr}) = \sum_{m=-\infty}^{+\infty} \exp[im(\theta_{kr} + \frac{\pi}{2})] J_m(kr),$$

we readily obtain:

$$(3.32) \quad \tilde{\varphi}_2(k, \theta_k) = \tilde{\varphi}_2(k) \cos(2\theta_k)$$

where:

$$(3.33) \quad \tilde{\varphi}_2(k) = -2\pi \int_0^\infty dr r \varphi_2(r) J_2(kr).$$

Remarkably, we see that the Fourier transform of the wavefunction vanishes along the *nodal* directions:

$$(3.34) \quad \theta_k = \pm \frac{\pi}{4},$$

while it is sizable along the *antinodal* directions:

$$(3.35) \quad \theta_k = 0, \pm \frac{\pi}{2}.$$

These features are reminiscent of the observed pseudogap in the underdoped region. Therefore, we are lead to identify $\Delta_2(\delta)$ with the pseudogap and to introduce the pseudogap temperature according to:

$$(3.36) \quad k_B T^*(\delta) = \frac{1}{2} \Delta_2(\delta).$$

3.2. Superconductivity in the underdoped region and the pseudogap. – We have shown in the previous Section that, as long as $\delta < \delta^*$, it is energetically favored to pair two holes into a d-wave bound state with wavefunction given by Eq. (3.29). Then, we may construct the superconducting ground state according to Eq. (3.1) with $\varphi(\vec{r}_i - \vec{r}_j) = \varphi_2(\vec{r}_i - \vec{r}_j)$. However, although the formation of Cooper pairs is essential in forming the superconducting state, its remarkable properties, i.e. zero resistance and perfect diamagnetism, require phase coherence among the pairs. In the underdoped region $\delta \ll \delta^*$ we infer from Fig. 4 that the size of the pair is small with respect to the average distance between holes. So that the ground state wavefunction Eq. (3.1) reduces to the ground state of a Bose-Einstein gas of paired holes. In this case the required phase coherence is established by the condensation of pairs. However, in two spatial dimensions it is well known that there is no Bose-Einstein condensation. Thus we are lead to conclude that in the extremely underdoped region $\delta \ll \delta^*$ there is a pseudogap $\Delta_2(\delta)$ but not superconductivity. However, by increasing δ it will be a certain minimal value of the hole doping fraction δ_{min} where the pairs become to overlap. To estimate δ_{min} , we observe that the pair wavefunction $\varphi_2(r)$ extends up to distance $r \sim \xi_0 \simeq 6a_0$. Thus, to have overlap between different hole pairs we need at least two holes in a square of size $6a_0$. Thereby we estimate:

$$(3.37) \quad \delta_{min} \simeq \frac{2}{6^2} \simeq 0.056,$$

which agrees, remarkably, with the observed value $\delta_{min} \simeq 0.05 - 0.06$ for the onset of the superconductivity in the hole-doped cuprates. Once the pairs begin to overlap, the phases of the pairs are locked to a constant value. Indeed, it is well known⁽⁴⁾ that a condensate with varying phase $\Theta(\vec{R})$ contribute to the ground state energy with:

$$(3.38) \quad H_\Theta = \frac{K_s}{2} \int d\vec{R} |\nabla\Theta(\vec{R})|^2,$$

where K_s is the so-called phase stiffness. In our case we have:

$$(3.39) \quad K_s \simeq \frac{\hbar^2}{2m_h^*} n_s$$

with the superfluid density given by:

$$(3.40) \quad n_s \simeq \frac{\delta}{2a_0^2}, \quad \delta_{min} \leq \delta.$$

As is well known [31, 32], the phase coherence of the condensate survives up to the

⁽⁴⁾ For instance, see Ref. [30].

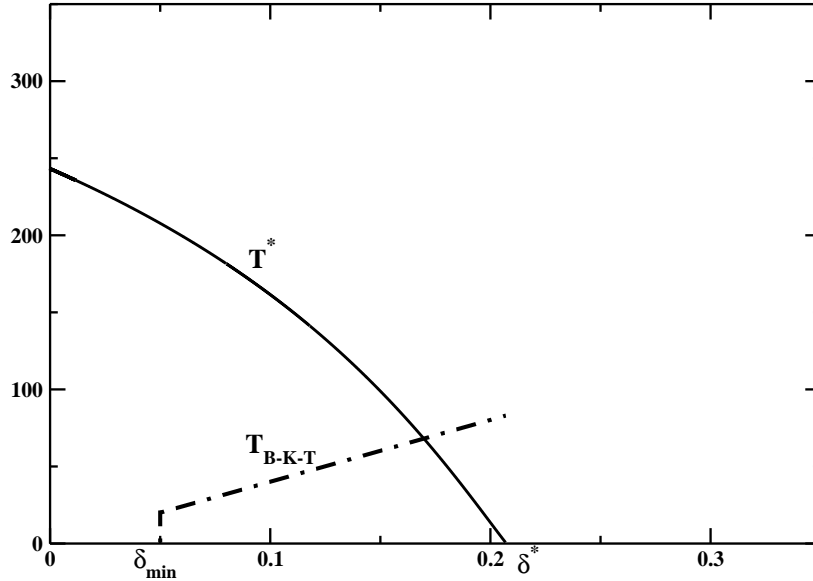


Fig. 5. – The pseudogap and Berezinskii-Kosterlitz-Thouless temperatures (in Kelvin) versus δ . We assume $\delta_{min} \simeq 0.05$.

Berezinskii-Kosterlitz-Thouless (B-K-T) critical temperature:

$$(3.41) \quad k_B T_{B-K-T} \simeq \frac{\pi}{2} K_s(T_{B-K-T}).$$

For temperatures above T_{B-K-T} the phase coherence and the superconductivity is lost due to the thermal activation of vortex excitations. If we neglect the temperature dependence of the phase stiffness, we obtain:

$$(3.42) \quad k_B T_{B-K-T} \simeq \frac{\pi}{8} \frac{\hbar^2}{m_h^*} \frac{\delta}{a_0^2} \simeq \pi \frac{t^2}{U} \delta, \quad \delta_{min} \leq \delta.$$

Using our numerical values for t and U we get:

$$(3.43) \quad T_{B-K-T} \simeq 401 K \delta, \quad \delta_{min} \leq \delta.$$

In Figure 5 we display the Berezinskii-Kosterlitz-Thouless critical temperature together with the pseudogap temperature T^* versus the hole doping fraction by assuming $\delta_{min} \simeq 0.05$. We see that in our approach the superconductivity transition in the underdoped region is described by the $B-K-T$ transition at $T_c = T_{B-K-T}$, which coexists with the much higher pseudogap temperature T^* . This picture is supported by a large amounts of observational data which, however, will be discussed in details in Sect. 4.

3.3. *d*-wave BCS ground state. – To complete the phase diagram of the hole-doped cuprate superconductors we must address the problem of the ground state for $\delta > \delta^*$. Since the pseudogap $\Delta_2(\delta)$ vanishes at $\delta = \delta^*$, we do not have real-space paired holes

and, whence, the $B - K - T$ critical temperature cannot be defined. On the other hand, as long as $\delta < \delta_c \simeq 0.35$, the attractive two-body potential Eq. (2.7) is short-range and can be considered as a small perturbation. As a consequence, in the overdoped region $\delta > \delta^*$ the normal state is described by the Hamiltonian \hat{H}_0 , Eq. (2.18). In other words, the normal state properties are those of ordinary Fermi liquid metals that is characterized by hole quasiparticles with effective mass given by Eq. (2.17) and density:

$$(3.44) \quad n_h \simeq \frac{1 + \delta}{a_0^2} .$$

In fact, in the overdoped side of the superconducting phase diagram, experiments strongly suggest that above the critical temperature the full Fermi surface is restored with well-defined quasiparticles. Thereby this confirms the applicability of a Fermi liquid picture. Moreover, quantum oscillation experiments [33] in an overdoped high-temperature superconductor are consistent with hole quasiparticles with density given by Eq. (3.44) and effective mass:

$$(3.45) \quad m_h^* = (4.1 \pm 1.0) m_e$$

in fair agreement with our estimate, Eq. (2.19).

The superconductive instability is driven by the short-range attractive interaction between the quasiparticles. We see, then, that the pairing is in momentum space, so that the relevant superconducting ground state is the BCS variational ground state Eq. (3.9) with Hamiltonian $\hat{H} - \mu\hat{N}$, where the chemical potential is essentially the Fermi energy:

$$(3.46) \quad \mu \simeq \varepsilon_F , \quad \varepsilon_F = \frac{\hbar^2 k_F^2}{2m_h^*} , \quad k_F \simeq \sqrt{2\pi n_h} .$$

The relevant gap equation has been discussed since long time [34]:

$$(3.47) \quad \Delta(\vec{k}) = -\frac{1}{2} \sum_{\vec{k}'} \frac{V(\vec{k} - \vec{k}') \Delta(\vec{k}')}{\sqrt{\xi_{\vec{k}'}^2 + |\Delta(\vec{k}')|^2}}$$

where:

$$(3.48) \quad \xi_{\vec{k}} = \frac{\hbar^2 \vec{k}^2}{2m_h^*} - \varepsilon_F$$

and

$$(3.49) \quad V(\vec{k} - \vec{k}') = \int d\vec{r} \exp[-i(\vec{k} - \vec{k}') \cdot \vec{r}] V(r) .$$

Using the expansion Eq. (3.31) we may recast Eq. (3.47) into:

$$(3.50) \quad \Delta(\vec{k}) = -\frac{1}{2} \sum_{\vec{k}'} \sum_{m=-\infty}^{+\infty} \exp(im\theta_{kk'}) \frac{V_m(k, k') \Delta(\vec{k}')}{\sqrt{\xi_{\vec{k}'}^2 + |\Delta(\vec{k}')|^2}} ,$$

with:

$$(3.51) \quad V_m(k, k') = 2\pi \int_0^\infty dr r V(r) J_m(kr) J_m(k'r) .$$

Equation (3.50) suggests that:

$$(3.52) \quad \Delta(\vec{k}) = \Delta(k, \theta_k) = \sum_{\ell=-\infty}^{+\infty} \exp(i\ell\theta_k) \Delta_\ell(k) ,$$

In the weak coupling limit one expects that the mixing of different partial wave ℓ will be small [34]. Therefore Eq. (3.50) reduces to:

$$(3.53) \quad \Delta_m(k, \theta_k) \simeq -\frac{1}{2} \sum_{\vec{k}'} \exp(im\theta_{kk'}) \frac{V_m(k, k') \Delta_m(k', \theta_{k'})}{\sqrt{\xi_{\vec{k}'}^2 + |\Delta_m(k', \theta_{k'})|^2}} .$$

Since the BCS gap in the limit of localized pairs is proportional to the bound-state wave function in momentum space, we conclude that Eq. (3.53) admits non trivial solutions for the d-wave gap ($m = \pm 2$). Moreover, from Eq. (3.32) we infer that:

$$(3.54) \quad \Delta_2(k, \theta_k) \equiv \Delta_{BCS}(k, \theta_k) = \Delta_{BCS}(k) \cos(2\theta_k) .$$

Thus, we obtain the following gap equation:

$$(3.55) \quad \Delta_{BCS}(k) \simeq - \sum_{\vec{k}'} [\cos(2\theta_{k'})]^2 \frac{V_2(k, k') \Delta_{BCS}(k')}{\sqrt{\xi_{\vec{k}'}^2 + [\Delta_{BCS}(k') \cos(2\theta_{k'})]^2}} .$$

Since the gap is sizable on the Fermi surface, we may further simplify Eq. (3.55) as:

$$(3.56) \quad 1 \simeq -V_2 \int \frac{d\vec{k}'}{(2\pi)^2} \frac{[\cos(2\theta_{k'})]^2}{\sqrt{\xi_{\vec{k}'}^2 + [\Delta_{BCS} \cos(2\theta_{k'})]^2}}$$

where $\Delta_{BCS} = \Delta_{BCS}(k_F)$ and $V_2 = V_2(k_F, k_F)$. A standard calculation gives:

$$(3.57) \quad 1 \simeq -\frac{V_2 m_h^*}{\hbar^2} \int_{-\varepsilon_c}^{+\varepsilon_c} \frac{d\xi}{(2\pi)^2} \int_0^{2\pi} d\theta \frac{[\cos(2\theta)]^2}{\sqrt{\xi^2 + [\Delta_{BCS} \cos(2\theta)]^2}}$$

where ε_c is an energy cut-off much smaller than the Fermi energy. Performing the integrals and using the approximation:

$$(3.58) \quad \operatorname{arcsinh} \left[\frac{\varepsilon_c}{\Delta_{BCS} |\cos(2\theta)|} \right] \simeq \ln \left[\frac{2\varepsilon_c}{\Delta_{BCS} |\cos(2\theta)|} \right] ,$$

we get:

$$(3.59) \quad \Delta_{BCS} \simeq \frac{4\varepsilon_c}{\sqrt{e}} \exp \left[-\frac{1}{\lambda_2} \right] ,$$

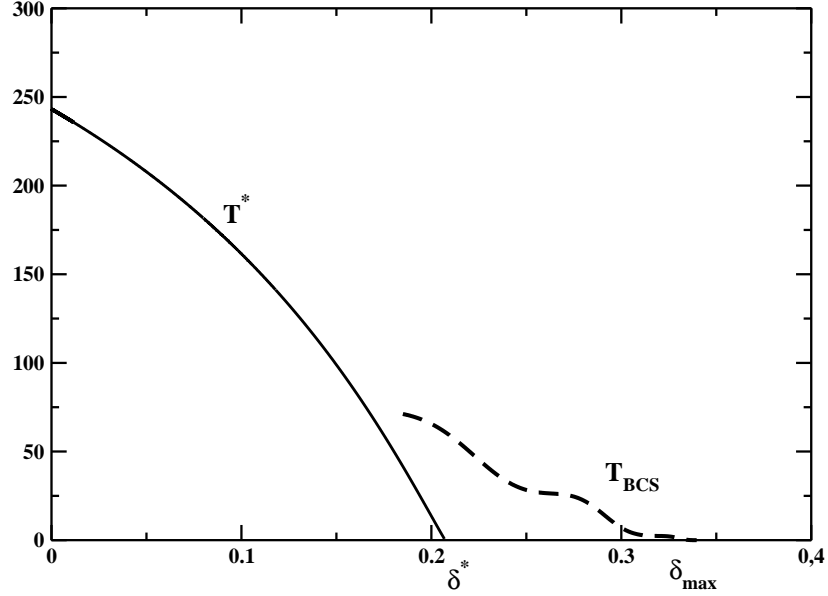


Fig. 6. – The pseudogap and BCS critical temperatures (in Kelvin) versus the hole doping fraction.

where:

$$(3.60) \quad \lambda_2 = \frac{m_h^* V_0}{\hbar^2} \int_0^{r_0(\delta)} dr r [J_2(k_F r)]^2 .$$

To obtain the critical temperature, we note that [35]:

$$(3.61) \quad \frac{\Delta_{BCS}}{k_B T_c} \simeq \pi e^{\ln 2 - \frac{1}{2} - \gamma} ,$$

$\gamma = 0.577216\dots$ being the Euler's constant. As concern the high-energy cut-off, it is natural to identify ε_c with $\Delta_2(\delta = 0)$ which, indeed, is much smaller than the Fermi energy in the range of hole doping fraction of interest. In summary, we obtain for the critical temperature $T_c \equiv T_{BCS}$:

$$(3.62) \quad k_B T_{BCS} \simeq \frac{2e^\gamma}{\pi} \Delta_2(0) \exp\left[-\frac{1}{\lambda_2}\right] .$$

Equation (3.62) shows that the BCS critical temperature depends on the hole doping fraction. In fact, in Fig. 6 we compare $T_{BCS}(\delta)$ with the pseudogap temperature $T^*(\delta)$. It is evident that for $\delta^* \leq \delta \leq \delta_{max} \simeq 0.30$ we have a non-zero BCS d-wave gap. Note that the undulations on the critical temperature curve is an artifact of the sharp cut-off of the effective interaction potential at $r = r_0(\delta)$.

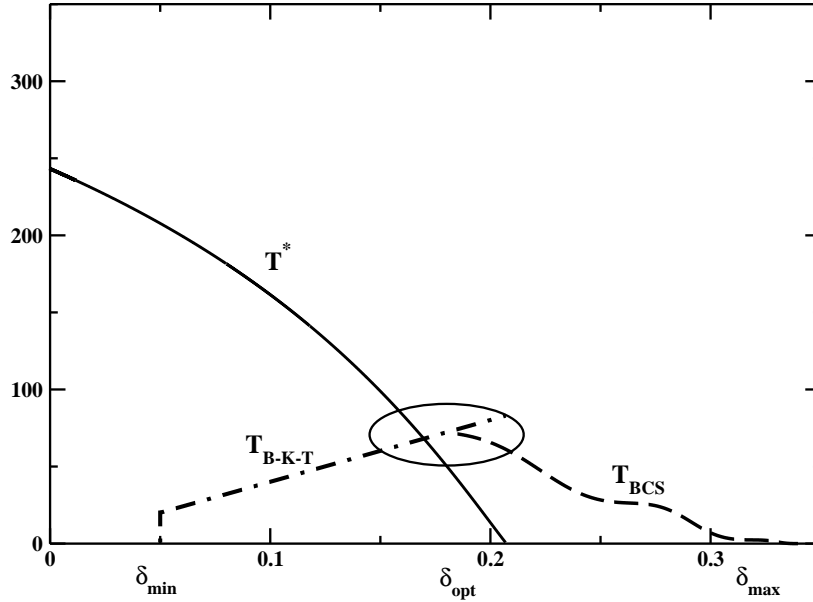


Fig. 7. – The pseudogap, Berezinskii-Kosterlitz-Thouless, and BCS critical temperatures (in Kelvin) versus the hole doping fraction δ . The region enclosed by the ellipse where the three temperatures are comparable is the optimal doped region.

3.4. Phase diagram of hole-doped cuprates. – We are, now, in position of discuss the phase diagram of the hole-doped cuprates. In Fig. 7 we display the Berezinskii-Kosterlitz-Thouless (T_{B-K-T}), the pseudogap (T^*), and the BCS (T_{BCS}) temperatures versus the hole doping fraction δ . In our approach the superconducting dome-shaped region of the phase diagram of oxide cuprates is determined by the region enclosed by the two critical temperatures T_{B-K-T} and T_{BCS} . The Berezinskii-Kosterlitz-Thouless temperature increases with the doping δ , while the BCS critical temperature decreases with increasing hole doping. These temperatures are comparable for $\delta \sim \delta_{opt}$. Accordingly, we individuate three regions in the phase diagram:

- the underdoped region $\delta_{min} \lesssim \delta < \delta_{opt}$;
- the optimal doped region $\delta \approx \delta_{opt}$;
- the overdoped region $\delta_{opt} < \delta \lesssim \delta_{max}$.

In Fig. 7 we have also displayed the pseudogap temperature $T^*(\delta)$ which decreases rapidly with increasing doping, meets the superconducting dome in the optimal doped region, and vanishes beyond a critical doping level δ^* within the optimal doped region. In the following Sections we shall discuss the physical properties which characterize the three regions and compare with selected experimental observations supporting our proposal.

4. – The physics of the underdoped region

The underdoped region in all hole-doped high-temperature superconductors is characterized by the presence of the pseudogap ⁽⁵⁾. In general it is assumed that the pseudogap has a d-wave structure. Moreover, there is a general agreement on the doping dependence of the pseudogap. For instance, recently the authors of Ref. [38] used angle resolved photoemission spectroscopy to probe the electronic excitations in underdoped $Bi_2Sr_2CaCu_2O_{8+\delta}$. These authors find evidence of a nodal liquid whose excitation gap vanishes only at points in momentum space which are consistent with the gap structure of a d-wave superconductors. In particular, these authors show that the measured gap in momentum space is consistent with:

$$(4.1) \quad \Delta_2(\delta, \theta_k) = \Delta_2(\delta) \cos(2\theta_k),$$

where $\Delta_2(\delta)$ monotonically increase with underdoping. In fact, Eq. (4.1) is consistent with our Eq. (3.32) and the doping dependence of the pseudogap (see Fig. 3). However, it should be stressed that many experiments report a gap that deviates from the simple relation in Eq. (4.1) [39, 40, 41, 42, 43, 44, 45, 46]. In fact, several experimental studies are consistent with the presence of two gaps, namely the pseudogap and a peculiar nodal gap. We believe that this nodal gap is related to the dynamics of the nodal Fermi liquid discussed in Sect. 4.4. Then, we see that the nodal gap has naturally a d-wave symmetry with gapless nodes. On the other hand, the pseudogap being defined as the energy needed to break the real-space two-hole bound state, does not need to depend on the geometry of the Fermi surface. However, a full account on this subject lies beyond the aim of the present paper. We plan to present a detailed discussion of this point in a separate paper. As concern the pseudogap temperature, in Fig. 8, where we plot $\frac{T_c^*}{T_c}$ versus $\frac{2\Delta_2}{k_B T^*}$ for various cuprates [47], we compare the experimental data with our relation Eq. (3.36) which can be rewritten as:

$$(4.2) \quad \frac{2\Delta_2}{k_B T^*} = 4.0.$$

Indeed, we see that the data are consistent with Eq. (4.2). We also plot in Fig. 8 the d-wave BCS relation ⁽⁶⁾:

$$(4.3) \quad \frac{2\Delta_2}{k_B T^*} \simeq 4.3.$$

Since Eq. (4.3) is quite close to our Eq. (4.2), the data are consistent with both relations. In our opinion, this unfortunate circumstance is the origin of confusion and several misinterpretations in the literature.

In conclusion, according to our previous discussion, the observed gap opening in the density of states (the pseudogap) marks the onset of the hole pairing at rather high temperatures $T \lesssim T^*$, but the critical temperature is set by the onset of phase coherence at lower temperatures $T \lesssim T_c = T_{B-K-T}$. The above point of view is supported by several experiments. We believe that the most convincing evidence comes from Ref. [48]. In

⁽⁵⁾ For a review on the pseudogap in cuprates, see Refs. [36, 37].

⁽⁶⁾ The d-wave BCS critical temperature will be discussed in Sect. 5.

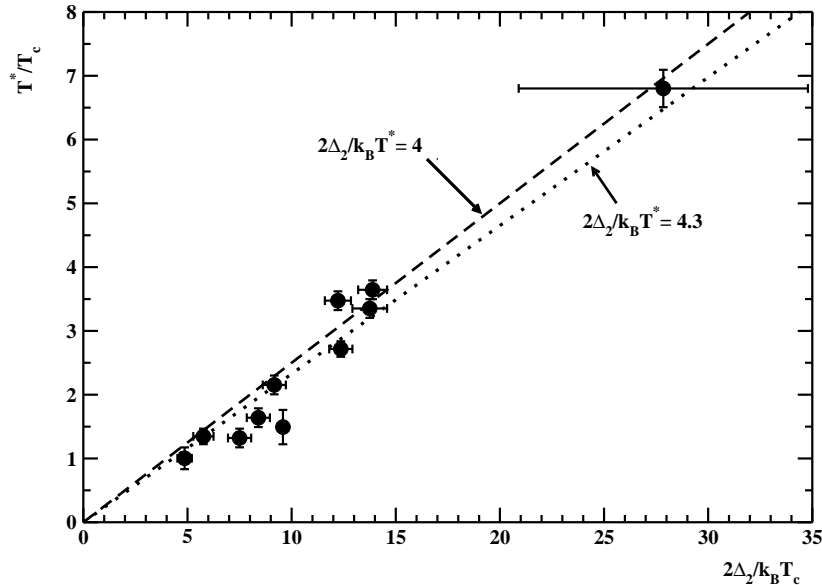


Fig. 8. – $\frac{T^*}{T_c}$ versus $\frac{2\Delta_2}{k_B T_c}$ for various cuprates compared to our relation $\frac{2\Delta_2}{k_B T^*} = 4$ (dashed line) and the d-wave BCS relation $\frac{2\Delta_2}{k_B T^*} = 4.3$ (dotted line). The data have been extracted from Fig. 5 of Ref. [47].

fact, by using ultrathin films of Ca-substituted $YBa_2Cu_3O_{7-\delta}$, the authors of Ref. [48] found a clear evidence of the Berezinskii-Kosterlitz-Thouless transition. In particular, they observe a remarkable scaling of the critical temperature with n_s in accordance with Eqs. (3.39) and (3.41). Further support on this picture comes from measurements of the high-frequency conductivity reported in Ref. [49].

To summarize, we may conclude that the key features of the underdoped side of the phase diagram are controlled by very strong hole pairing that is phase-disordered by fluctuations [50]. In the following subsections, from a wealth of possible material, we have chosen to discuss some selected topics that we think well illustrate the physics of the underdoped region of hole-doped high-temperature superconductors.

4.1. Real space bound state in magnetic fields. – We are interested in the dynamics of hole pairs in presence of an external magnetic field perpendicular to the copper-oxide plane:

$$(4.4) \quad \vec{H} = \nabla \times \vec{A} \quad , \quad \vec{A} = (A_1(\vec{r}), A_2(\vec{r}), 0) .$$

In this case the Schrödinger equation Eq. (3.11) becomes:

$$(4.5) \quad \left[\frac{1}{2m_h^*} \left(-i\hbar\nabla_{\vec{r}_1} - \frac{e}{c}\vec{A}(\vec{r}_1) \right)^2 + \frac{1}{2m_h^*} \left(-i\hbar\nabla_{\vec{r}_2} - \frac{e}{c}\vec{A}(\vec{r}_2) \right)^2 \right] \Phi(\vec{r}_1, \vec{r}_2) + V(\vec{r}_1 - \vec{r}_2) \Phi(\vec{r}_1, \vec{r}_2) = E\Phi(\vec{r}_1, \vec{r}_2) .$$

It is useful to work in the symmetric gauge:

$$(4.6) \quad \vec{A} = -\frac{1}{2} \vec{r} \times \vec{H} ,$$

where the angular momentum is conserved. Using Eq. (3.12) we recast Eq. (4.5) into:

$$(4.7) \quad \left[\frac{1}{4m_h^*} \left(-i\hbar\nabla_{\vec{R}} - \frac{2e}{c} \vec{A}(\vec{R}) \right)^2 + \frac{1}{m_h^*} \left(-i\hbar\nabla_{\vec{r}} - \frac{e}{2c} \vec{A}(\vec{r}) \right)^2 \right] \Phi(\vec{R}, \vec{r}) + V(\vec{r}) \Phi(\vec{R}, \vec{r}) = E\Phi(\vec{R}, \vec{r}) .$$

Thus, we can write:

$$(4.8) \quad \Phi(\vec{R}, \vec{r}) = \Psi(\vec{R}) \varphi(\vec{r}) ,$$

and

$$(4.9) \quad E = E_{cond} - \Delta ,$$

such that:

$$(4.10) \quad \frac{1}{4m_h^*} \left[-i\hbar\nabla_{\vec{R}} - \frac{2e}{c} \vec{A}(\vec{R}) \right]^2 \Psi(\vec{R}) = E_{cond} \Psi(\vec{R}) ,$$

$$(4.11) \quad \left[\frac{1}{m_h^*} \left(-i\hbar\nabla_{\vec{r}} - \frac{e}{2c} \vec{A}(\vec{r}) \right)^2 + V(\vec{r}) \right] \varphi(\vec{r}) = -\Delta \varphi(\vec{r}) .$$

The wavefunction $\Psi(\vec{R})$ describes the condensate. In fact, $\Psi(\vec{R})$ is obtained from $\Phi(\vec{R}, \vec{r})$ after averaging over the internal degree of freedom. Moreover, if we write:

$$(4.12) \quad \Psi(\vec{R}) = |\Psi(\vec{R})| \exp[i\Theta(\vec{R})] ,$$

we see that in presence of an external magnetic field the condensate acquires a non-uniform phase. For an almost uniform condensate we have:

$$(4.13) \quad |\Psi(\vec{R})| = \text{constant} ,$$

and $\Theta(\vec{R})$ is a slowly varying function. In this case we obtain:

$$(4.14) \quad E_{cond} \simeq \frac{1}{2} (2m_h^*) \vec{v}_s^2(\vec{R}) ,$$

where the supercurrent velocity is given by the well-known relation [51]:

$$(4.15) \quad 2m_h^* \vec{v}_s(\vec{R}) = \hbar \nabla_{\vec{R}} \Theta(\vec{R}) - \frac{2e}{c} \vec{A}(\vec{R}) .$$

Let us, now, consider Eq. (4.11) in polar coordinates:

$$(4.16) \quad \left[\frac{-\hbar^2}{m_h^*} \left(\frac{\partial^2}{\partial r^2} + \frac{1}{r} \frac{\partial}{\partial r} + \frac{1}{r^2} \frac{\partial^2}{\partial \theta^2} \right) + \frac{e^2 H^2}{16m_h^* c^2} r^2 + \frac{ie\hbar H}{2m_h^* c} \frac{\partial}{\partial \theta} + V(r) \right] \varphi(r, \theta) = -\Delta \varphi(r, \theta) .$$

Again, after writing:

$$(4.17) \quad \varphi(r, \theta) = \frac{\exp(im\theta)}{\sqrt{2\pi}} \varphi_m(r) ,$$

we have:

$$(4.18) \quad \left[\frac{-\hbar^2}{m_h^*} \left(\frac{d^2}{dr^2} + \frac{1}{r} \frac{d}{dr} - \frac{m^2}{r^2} \right) + \frac{e^2 H^2}{16m_h^* c^2} r^2 + V(r) \right] \varphi_m(r) = -(\Delta_m(H) + \frac{e\hbar m H}{2m_h^* c}) \varphi_m(r)$$

This last equation shows that, as expected, the external magnetic field lifts the degeneracy $m \rightarrow -m$.

4.2. *The upper critical magnetic field H_{c2} .* – We have already seen that for $H = 0$ two holes give rise to a d-wave bound state. In presence of an external magnetic field the d-wave bound states are the solutions of our pervious Eq. (4.18) specialized to $m = \pm 2$:

$$(4.19) \quad \left[\frac{-\hbar^2}{m_h^*} \left(\frac{d^2}{dr^2} + \frac{1}{r} \frac{d}{dr} - \frac{4}{r^2} \right) + \frac{e^2 H^2}{16m_h^* c^2} r^2 + V(r) \right] \varphi_{\pm 2}(r) = -(\Delta_{\pm 2}(H) \pm \frac{e\hbar H}{m_h^* c}) \varphi_{\pm 2}(r) .$$

We may, now, introduce the pair-breaking critical field H_{c2}^{pb} such that:

$$(4.20) \quad \Delta_{\pm 2}(H_{c2}^{pb}, \delta) = 0 .$$

To estimate the pair-breaking critical magnetic field we note that:

$$(4.21) \quad \Delta_{\pm 2}(0, \delta) = \Delta_2(\delta) ,$$

where the pseudogap $\Delta_2(\delta)$, already discussed in Sect. 3.1, can be approximated quite accurately by:

$$(4.22) \quad \Delta_2(\delta) \simeq \Delta_2(0) \left[1 - \left(\frac{\delta}{\delta^*} \right)^{1.5} \right] , \quad \Delta_2(0) \simeq 41.91 \text{ meV} .$$

Moreover, it is easy to see that the Zeeman term can be neglected. In fact, using Eq. (2.19) we find:

$$(4.23) \quad \frac{e\hbar H}{m_h^* c} \simeq 2.14 \cdot 10^{-5} \text{ eV } H(T) ,$$

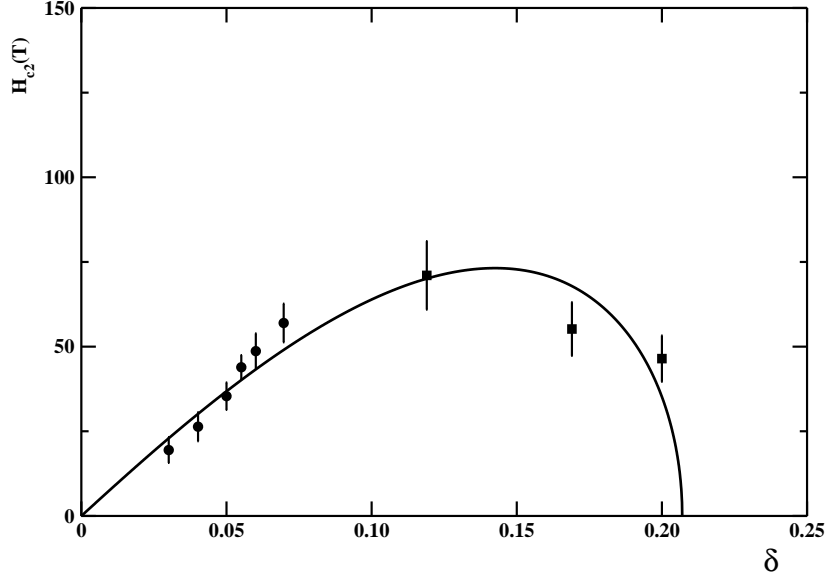


Fig. 9. – The upper critical field H_{c2} versus the hole doping fraction δ according to Eq. (4.31) assuming $\kappa \simeq 1.3 \cdot 10^2$. The data have been extracted from Fig. 18 of Ref. [52] (full squares) and Fig. 4 of Ref. [53] (full circles).

where $H(T)$ means that the strength of the magnetic field is measured in Tesla ⁽⁷⁾. Accordingly, we get from Eq. (4.19):

$$(4.24) \quad \Delta_{\pm 2}(H, \delta) \simeq \Delta_2(\delta) - \frac{e^2 H^2}{16m_h^* c^2} \langle r^2 \rangle .$$

Since $\langle r^2 \rangle \simeq \xi_0^2$, we obtain:

$$(4.25) \quad H_{c_2}^{pb} \simeq \sqrt{\frac{16m_h^* c^2}{e^2 \xi_0^2} \Delta_2(\delta)} ,$$

which leads to:

$$(4.26) \quad H_{c_2}^{pb} \simeq 1.90 \cdot 10^3 T \sqrt{1 - \left(\frac{\delta}{\delta^*}\right)^{1.5}} .$$

Equation (4.26) shows that the pair-breaking critical field is very high. This means that the pseudogap is not affected by applied magnetic fields $H \lesssim 10^2 T$ in accordance with several experimental observations.

In conventional superconductors the pair-breaking critical field is of the same order of

⁽⁷⁾ $1T = 10^4 G$. Even though we are using CGS units, it is customary in the literature to express the applied magnetic field in Tesla.

the depairing critical field. In our case, it turns out that the depairing critical field is much smaller than the pair-breaking critical field. As a consequence, the upper critical field H_{c_2} is determined by the depairing field. It is worthwhile to recall that in type-II superconductors in the mixed state (Schubnikov phase) between the lower critical field H_{c_1} and the upper critical field H_{c_2} , the magnetic flux penetrates in a regular array of flux tubes, each carrying a quantum flux:

$$(4.27) \quad \phi_0 = \frac{2\pi\hbar c}{2e} \simeq 2.07 \cdot 10^{-7} \text{ G cm}^2 .$$

Within each unit cell of the array there is a vortex of supercurrent concentrating the flux toward the vortex center. To estimate the critical velocity \vec{v}_c we use Eqs. (4.9) and (4.14) to get:

$$(4.28) \quad E_{cond} \simeq m_h^* \vec{v}_c^2 \simeq \Delta_2(H, \delta) \simeq \Delta_2(\delta) .$$

Accordingly, the critical supercurrent is:

$$(4.29) \quad \vec{J}_c = 2 e n_s \vec{v}_c \simeq e \frac{\delta}{a_0^2} \vec{v}_c .$$

From the Maxwell equation $\nabla \times \vec{H} = \frac{4\pi}{c} \vec{J}$ we easily get the following estimate:

$$(4.30) \quad H_{c_2} \simeq \frac{4\pi}{c} |\vec{J}_c| \simeq \frac{4\pi}{c} \frac{e\delta}{a_0^2} \sqrt{\frac{\Delta_2(\delta)}{m_h^*}} .$$

Since the magnetic field can be considered almost uniform over distance of order of the London penetration length λ , and considering that there are $N_{vort} \simeq (\frac{\lambda}{\xi})^2 = \kappa^2$ vortices in a region of area λ^2 , we obtain our final estimate of the upper critical field:

$$(4.31) \quad H_{c_2}(\delta) \simeq \kappa^2 \frac{4\pi}{c} \frac{e\delta}{a_0^2} \sqrt{\frac{\Delta_2(\delta)}{m_h^*}} .$$

In Fig. 9 we display our estimate of the upper critical field Eq. (4.31) in the underdoped region $\delta < \delta^*$. We see that in the deep underdoped region the upper critical field decreases with underdoping in accordance with recent measurements [52, 53, 54]. In Fig. 9 we also display the depairing critical field as determined from the Nernst signal in Refs. [52, 53]. It is known that the cuprate superconductors have a large Ginzburg-Landau parameter $\kappa \sim 10^2$ and are, therefore, extreme type-II superconductors. In fact, to compare quantitatively Eq. (4.31) with experimental data we choose $\kappa \simeq 130$. It is gratifying to see that the doping dependence of our critical magnetic field as implied by Eq. (4.31) seems to follow quite closely the experimental data.

4.3. The vortex region. – In the underdoped region of the high-temperature cuprate superconductors there is convincing evidence for vortices at temperatures significantly above the critical temperature [52, 53, 55, 56]. Indeed, our previous determination of the upper critical magnetic field shows that $H_{c_2}(\delta)$ is different from zero even for $\delta < \delta_{min} \simeq 0.05$, i.e. outside the superconducting dome in the phase diagram. To strengthen

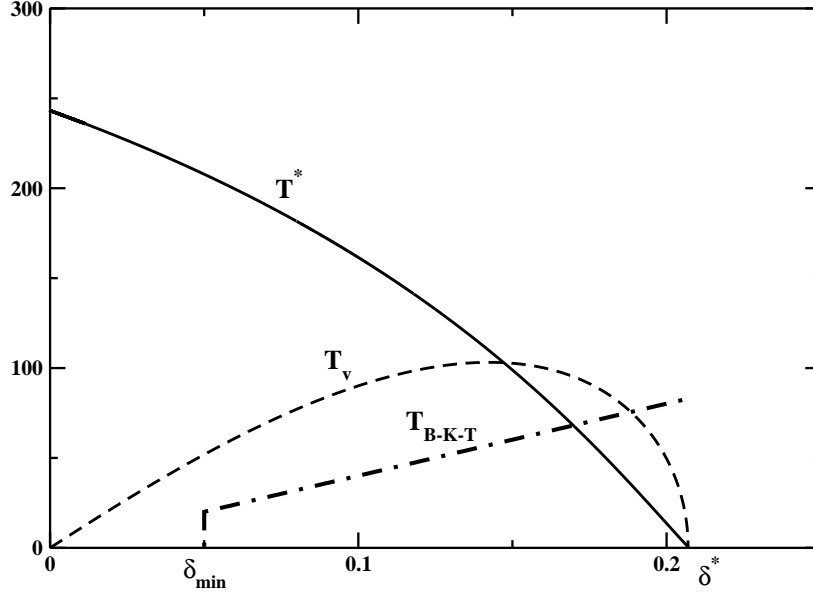


Fig. 10. – The pseudogap, Berezinskii-Kosterlitz-Thouless, and vortex temperatures (in Kelvin) versus δ . The vortex region lies in between T_V and T_{B-K-T} .

this point, following Ref. [57], we define a critical vortex temperature $T_V(\delta)$ by the phenomenological relation:

$$(4.32) \quad k_b T_V(\delta) \simeq 2.1 \mu_B H_{c_2}(\delta)$$

where μ_B is the Bohr magneton. The meaning of $T_V(\delta)$ is that vortices are absent for $T > T_V(\delta)$. In Fig. 10 we compare the vortex temperature to the critical Berezinskii-Kosterlitz-Thouless and pseudogap temperatures. For temperatures $T_{B-K-T}(\delta) < T < T_V(\delta)$ (the so-called Nernst region) one should observe a large Nernst signal well above the superconducting critical temperature, in accordance with observations.

We would like to conclude this Section by addressing the puzzling observations of discrete core bound states in isolated vortices. In a classical paper [58], it was predicted the existence of electronic states bound to the core of an isolated vortex at energies below the superconducting gap in the case of s-wave BCS superconductors. Since the spacing of the discrete spectrum turns out to be very small, these bound states lead to a continuum which manifests itself as a zero-bias conductance peak in scanning tunneling spectroscopy measurements. In high-temperature superconductors the scanning tunneling spectroscopy of isolated vortices revealed striking electronic signatures which cannot be understood within the conventional BCS s-wave or d-wave theory ⁽⁸⁾. Indeed, the vortex cores give evidence of a pair of states with energy which scales with the superconducting gap and do not depend on the applied magnetic field. If we denote with E_{core} the energy of the vortex core states measured with respect to the zero-bias voltage, then

⁽⁸⁾ See Ref. [6] and references therein.

there is a simple relation between the state energy and the superconducting gap [6]:

$$(4.33) \quad E_{core} \simeq \pm 0.3 \Delta_p ,$$

where the slope were obtained by a linear fit to all data points, and Δ_p is the superconducting gap. We have already noted that the data are consistent with the relation (see Fig. 8):

$$(4.34) \quad \frac{2 \Delta_p}{k_B T^*} \simeq 4.3 ,$$

so that, using Eq. (4.2), we may rewrite Eq. (4.33) in terms of the pseudogap:

$$(4.35) \quad E_{core} \simeq \pm 0.32 \Delta_2 .$$

To interpret this last remarkable relation, we refer to the Schrödinger equation for the d-wave hole bound states in presence of an external magnetic field, Eq. (4.18) with $m = \pm 2$. We have shown that, neglecting the Zeeman splitting, $\Delta_{\pm 2}(H, \delta) \simeq \Delta_2(\delta)$. Thus, we infer that the pseudogap without the external magnetic field fixes the zero-bias voltage in the core of an isolated vortex. Moreover, from Eq. (4.18) it follows that there are two states whose energies measured with respect to the pseudogap are given by:

$$(4.36) \quad E_{core} = \pm \frac{e\hbar H_{core}}{m_h^* c} ,$$

where H_{core} is the magnetic field inside the vortex core. To estimate H_{core} , we note that the size of the isolated vortex can be determined by:

$$(4.37) \quad \xi_V^2 \simeq \frac{\hbar^2}{\frac{m_h^*}{2} \Delta_2} ,$$

where $\frac{m_h^*}{2}$ is the hole reduced mass. Thus, the magnetic field in the vortex core can be obtained from:

$$(4.38) \quad \pi \xi_V^2 H_{core} \simeq \phi_0 ,$$

i.e.

$$(4.39) \quad H_{core} \simeq \frac{2\pi\hbar c}{2e} \frac{1}{\pi \xi_V^2} .$$

Inserting Eqs. (4.39) and Eq. (4.37) into Eq. (4.36), we get:

$$(4.40) \quad E_{core} \simeq \pm \frac{1}{2} \Delta_2$$

which is in satisfying agreement with Eq. (4.35).

4.4. *Fermi arcs and quantum oscillations.* – The normal-state properties in the underdoped region of high-temperature cuprates are highly anomalous. It is now well-established by many angle-resolved photoemission studies ⁽⁹⁾ that low-energy excitations are characterized by Fermi arcs, namely truncate segments of a Fermi surface. The resistivity obeys $\rho \sim T$ over a wide range of temperatures in striking contrast to a Fermi-liquid law $\rho \sim T^2$, expected for a conventional metals. Moreover, several recent studies [9, 59, 60, 61, 62, 63] report unambiguous identification of quantum oscillations in high magnetic fields. Interestingly enough, the measured low oscillation frequencies reveals a Fermi surface made of small pockets. In fact, from the Luttinger’s theorem and the Onsager relation [64, 65] between the frequency and the cross-sectional area of the orbit, it turns out that the area of the pocket correspond to about 2 – 3 % of the first Brillouin zone area in sharp contrast to that of overdoped cuprates where the frequency corresponds to a large hole Fermi surface [63]. In addition, the authors of Ref. [66] reported the observation of a negative Hall resistance in the magnetic-field-induced normal state, which reveals that these pockets are electron-like rather than hole-like. More recently [67], experiments on the second harmonic quantum oscillations in underdoped high-temperature cuprates lead to the conclusion that there exists only a single underlying quasi-two dimensional Fermi surface pocket. Moreover, it turns out that the pocket is most likely associated with states near the nodal region of the Brillouin zone. This nodal pocket comprises quasielectron carrier to explain both the high field quantum oscillations with negative Hall and Seebeck [68] effect. Finally, the recent studies of $YBa_2Cu_3O_{6.56}$ at very high magnetic fields indicate that the specific heat exhibits the conventional temperature dependence and quantum oscillations expected for a Fermi liquid. Moreover, the magnetic field dependence of the quasiparticle density of states follows the \sqrt{H} behavior pointing to a d-wave superconducting gap. Thus, the specific heat data demonstrate the surprising coexistence of the signature of a Fermi liquid and a d-wave superconducting gap over the entire magnetic field range measured.

In the present Section we show that in our approach these features can be accounted for as a consequence of the pseudogap $\Delta_2(\delta)$. We have already seen that, in the underdoped region $\delta < \delta^*$, the holes are bound into pairs with k-space wavefunction given by Eq. (3.32). Even though the pair wavefunction vanishes along the nodal directions $k_x = \pm k_y$ ($\theta_k = \pm \frac{\pi}{4}$), there are not nodal low-lying hole excitations. This is due to the fact that the pairing of the holes is in the real space and not in momentum space. On the other hand, due to the rotational symmetry, we may freely perform rigid rotations of the pairs without spending energy. The rigid rotations of pairs is equivalent to hopping of electrons according to the hopping term in the Hamiltonian Eq. (1.1):

$$(4.41) \quad \hat{H}_0^{(e)} = -t \sum_{\langle i,j \rangle, \sigma} \left[\hat{c}_{i,\sigma}^\dagger \hat{c}_{j,\sigma} + \hat{c}_{j,\sigma}^\dagger \hat{c}_{i,\sigma} \right].$$

We may diagonalize this Hamiltonian by writing:

$$(4.42) \quad \hat{\psi}_e(\vec{k}, \sigma) = \frac{1}{\sqrt{M}} \sum_j \exp(-i\vec{k} \cdot \vec{r}_j) \hat{c}_{j,\sigma},$$

⁽⁹⁾ See Ref. [2] and references therein.

to get:

$$(4.43) \quad \hat{H}_0^{(e)} = \sum_{\vec{k}, \sigma} \varepsilon_{\vec{k}}^{(e)} \hat{\psi}_e^\dagger(\vec{k}, \sigma) \hat{\psi}_e(\vec{k}, \sigma),$$

$$(4.44) \quad \varepsilon_{\vec{k}}^{(e)} = -2t [\cos(k_x a_0) + \cos(k_y a_0)].$$

In the small-k limit we have:

$$(4.45) \quad \hat{H}_0^{(e)} = \sum_{\vec{k}, \sigma} \frac{\hbar^2 \vec{k}^2}{2m_e^*} \hat{\psi}_e^\dagger(\vec{k}, \sigma) \hat{\psi}_e(\vec{k}, \sigma),$$

where:

$$(4.46) \quad m_e^* = \frac{\hbar^2}{2t a_0^2} \simeq 2.17 m_e.$$

Since there are $1 - \delta$ electrons per *Cu* atoms, from the Hamiltonian Eq. (4.45) we may determine the electron Fermi energy:

$$(4.47) \quad \varepsilon_F^{(e)} = \frac{\hbar^2 (\vec{k}_F^{(e)})^2}{2m_e^*}, \quad a_0 k_F^{(e)} \simeq \sqrt{2\pi(1-\delta)}.$$

At first glance, one expects that the quasielectrons fill in momentum space the circle with radius $k_F^{(e)}$ (the electron Fermi circle). However, one should keep in mind that the hopping of electrons is possible thanks to the paired holes. Since in momentum space the wavefunction of a given pair is spread over a region around $k \sim \frac{1}{\xi_0}$, we see that the wavefunction of quasielectrons is likewise localized on a region in k-space around $\frac{1}{\xi_0}$. Thus, the quasielectrons do not have the needed coherence to propagate over large distances with a well defined momentum. However, this argument does not apply along the nodal directions where the momentum space hole-pair wavefunction vanishes. Therefore we are led to the conclusions that there are coherent quasielectrons that fill small circular sectors of the electron Fermi circle around the nodal directions $k_x = \pm k_y$. Thanks to the rotational symmetry, we have four circular sectors with the same area. Since the number of coherent quasielectrons is determined by the doping fraction of holes (assuming that all the holes are paired), we obtain (see Fig. 11):

$$(4.48) \quad \frac{\delta}{a_0^2} \simeq \frac{4 \times 2}{(2\pi)^2} \frac{1}{2} (k_F^{(e)})^2 \theta_{FA},$$

i.e.

$$(4.49) \quad \theta_{FA} \simeq \frac{\pi}{2} \frac{\delta}{1-\delta}.$$

We see, thus, that the Fermi surface is made by four Fermi arcs in agreement with the

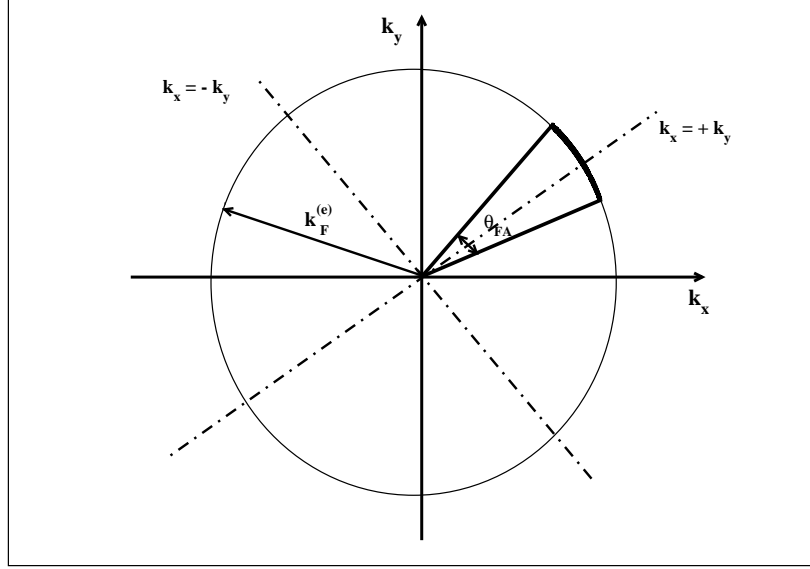


Fig. 11. – The Fermi sector and Fermi arc in the first quadrant of the Brillouin zone.

angle-resolved photoemission data. Moreover, the area of the Fermi sector with respect to the area of the Fermi circle in overdoped region turns out to be:

$$(4.50) \quad \frac{\mathcal{A}_{FA}}{\mathcal{A}_{overdoped}} \simeq \frac{1}{4} \frac{\delta}{1 + \delta} .$$

For the typical value of hole doping fraction $\delta \simeq 0.1$, we infer from Eq. (4.50) that \mathcal{A}_{FA} is about 2.3 % of the first Brillouin zone area in the overdoped region, in satisfying agreement with quantum oscillation experimental results. Note that the effective quasielectron mass measured in quantum oscillation experiments lies in the range $m_e^* = (2.0 - 3.0) m_e$, in agreement with our estimate Eq. (4.46).

The drastic reduction of the available states in momentum space leads to a peculiar quasielectron conductivity. To see this, we may employ the simple Drude model [70] for the frequency-dependent conductivity:

$$(4.51) \quad \sigma(\omega) \simeq \frac{\sigma_0}{1 - i\omega\tau} , \quad \sigma_0 = \frac{n_e e^2 \tau}{m_e^*} ,$$

where, according to Eq. (4.48), $n_e \simeq \frac{\delta}{a_0^2}$. Since the nodal quasielectrons suffer almost unidimensional scatterings, we get for the relaxation time the quite general estimate:

$$(4.52) \quad \frac{\hbar}{\tau} \sim \int_{\varepsilon_F^{(e)} - \varepsilon}^{\varepsilon_F^{(e)}} d\varepsilon' \sim \varepsilon \sim k_B T ,$$

and Eq. (4.51) becomes:

$$(4.53) \quad \sigma(\omega) \simeq \frac{\sigma_0}{1 - i \frac{\hbar\omega}{k_B T}} .$$

For $\hbar\omega \ll k_B T$ we obtain the conductivity:

$$(4.54) \quad \sigma \simeq \sigma_0 \simeq \frac{n_e e^2}{m_e^*} \frac{\hbar}{k_B T} \simeq \frac{e^2 \delta}{a_0^2 m_e^*} \frac{\hbar}{k_B T} .$$

On the other hand, if $\hbar\omega \gg k_B T$ we get:

$$(4.55) \quad \sigma(\omega) \simeq \frac{\sigma_0}{-i\omega\tau} \simeq i \frac{n_e e^2}{m_e^* \omega} \simeq i \frac{e^2 \delta}{a_0^2 m_e^*} \frac{1}{\omega} .$$

These relations are in qualitative agreement with several observations. In particular Eq. (4.54) should be valid up to temperatures of the order of the pseudogap temperature T^* .

Let us conclude this Section by discussing the peculiar dependence of the specific heat on the applied magnetic field reported in Ref. [69]. Firstly, we evaluate the Sommerfeld coefficient for $H = 0$. A standard calculation gives:

$$(4.56) \quad \gamma_s \simeq \frac{\delta}{1 - \delta} \frac{\pi}{3} \frac{m_e^* a_0^2}{\hbar^2} N_A k_B^2$$

where N_A is the Avogadro's number. The authors of Ref. [69] found that at very high magnetic fields the specific heat in an underdoped high-temperature superconductors exhibits both the conventional temperature dependence and quantum oscillations expected for a Fermi liquid. The oscillatory component of the specific heat is given by the Lifshitz-Kosevich formula [65]. On the other hand, for the Sommerfeld coefficient they report:

$$(4.57) \quad \gamma_s(H) = \gamma_s(H = 0) + A_c \sqrt{H} ,$$

with

$$(4.58) \quad \gamma_s(H = 0) = 1.85 \pm 0.06 \text{ mJ mol}^{-1} \text{ K}^{-2} , \quad A_c \simeq 0.47 \text{ mJ mol}^{-1} \text{ K}^{-2} \text{ T}^{-\frac{1}{2}} .$$

To compare our Eq. (4.56) with Eq. (4.58) one should keep in mind that there are two CuO_2 planes per formula unit in YBCO . Moreover, the planar CuO_2 densities in high-temperature cuprates are difficult to estimate. Assuming $\delta \simeq 0.1$ and using the effective electron mass Eq. (4.46), we find (in MKS units):

$$(4.59) \quad \gamma_s \simeq 0.76 \text{ mJ mol}^{-1} \text{ K}^{-2} ,$$

which differs from measured value in Eq. (4.58) by about a factor of 2. As far as field-induced Sommerfeld coefficient is concerned, the behavior $\gamma_s(H) \sim \sqrt{H}$ is interpreted as evidence of the presence of a d-wave superconducting gap. In fact, it was pointed out [71] that the increase of the Sommerfeld coefficient with the external magnetic field is due

to the line nodes of the superconducting gap. The evidence of quantum oscillations and field-induced Sommerfeld coefficient in the electronic specific heat points to the surprising coexistence of a Fermi liquid and a d-wave superconductor. In our approach, we now show that the quasielectron nodal Fermi liquid leads naturally to the observed Sommerfeld coefficient $\gamma_s(H) \sim \sqrt{H}$. In the mixed state, according to Ref. [71] the energies of the low-lying excitations circulating around a vortex are shifted by Doppler effect. Since it results that $k_F^{(e)} \xi_0 \gg 1$, we may employ the semiclassical approach which considers the momentum and position of quasiparticles as commuting variables. The effects of the supercurrent circulating around a vortex is accounted for by a Doppler shift of the quasiparticle energy. Thus, for the quasielectrons we have:

$$(4.60) \quad \varepsilon(\vec{k}, \vec{r}) \simeq \frac{\hbar^2 \vec{k}^2}{2 m_e^*} + \hbar \vec{k} \cdot \vec{v}_s(\vec{r}),$$

where $\vec{v}_s(\vec{r})$ is the supervelocity that, according to Eq. (4.15), is given by:

$$(4.61) \quad \vec{v}_s(\vec{r}) \simeq \frac{\hbar}{4 m_h^*} \frac{\hat{\theta}_r}{r}.$$

The Doppler shift Eq. (4.60) has a sizable effect on the density of state. To see this, we need to evaluate the density of state at the Fermi surface averaged over the vortex:

$$(4.62) \quad \mathcal{N}(0) \equiv 2 \int \frac{d\vec{k}}{(2\pi)^2} \int d\vec{r} \delta[\varepsilon(\vec{k}, \vec{r}) - \varepsilon_F^{(e)}] \frac{1}{\pi R^2},$$

where

$$(4.63) \quad R \simeq \xi_V \sqrt{\frac{H_{c2}}{H}}$$

is the average distance between vortices. We obtain:

$$(4.64) \quad \mathcal{N}(0) \simeq \frac{2}{4\pi^2} \int_{FA} d\theta_k \int_0^\infty dk k \int d\theta_r \int_{\xi_0}^R dr \frac{r}{\pi R^2} \delta \left[\frac{\hbar^2 k^2}{2m_e^*} - \frac{\hbar^2 k \sin(\theta_r + \theta_k)}{4m_e^* r} - \varepsilon_F^{(e)} \right]$$

where the angular integration on θ_k is performed over the four Fermi arcs (FA). The integration over k can be done easily. One obtains:

$$(4.65) \quad \mathcal{N}(0) \simeq \frac{1}{4\pi^2} \frac{(m_e^*)^2}{\hbar^2 m_h^*} \int_{FA} d\theta_k \int d\theta_r \int_{\xi_0}^R \frac{dr}{\pi R^2} \frac{\sin(\theta_r + \theta_k)}{k_F^{(e)}}.$$

Finally the angular integrations give:

$$(4.66) \quad \mathcal{N}(0) \simeq \frac{1}{4\pi^2} \frac{(m_e^*)^2}{\hbar^2 m_h^*} \frac{2\sqrt{2} \theta_{FA}}{\pi k_F^{(e)} R},$$

or, using Eqs. (4.63) and (4.49):

$$(4.67) \quad \mathcal{N}(0) \simeq \frac{\sqrt{2}}{4\pi^2} \frac{\delta}{1-\delta} \frac{(m_e^*)^2}{\hbar^2 m_h^*} \frac{1}{k_F^{(e)} R} \sqrt{\frac{H}{H_{c2}}} .$$

Since the high-temperature superconductors are extreme type-II superconductors, one should average the density of state over the vortex distribution. However, from Eq. (4.67) it is evident that the quasiparticle energy Doppler shift induced by vortices leads to the expected field-induced Sommerfeld coefficient $\gamma_s(H) \sim \sqrt{H}$.

5. – The physics of the over and optimal doped regions

In the overdoped region we have already stressed that the normal state properties can be described reasonably well by the Fermi liquid picture, although still with some electronic correlations, with a hole density corresponding to $1 + \delta$ holes per *Cu* atom. Indeed, as long as $\delta > \delta^*$, the effective two-body potential Eq. (2.7) can be dealt with as a small perturbation. Therefore, the dynamics of the copper-oxide layers is governed essentially by our effective Hamiltonian \hat{H}_0 , Eq. (2.18). Note that the correlation effects due to the on-site repulsion U are built into \hat{H}_0 by means of the effective hole mass m_h^* . It is interesting to note that:

$$(5.1) \quad \frac{m_h^*}{m_e^*} = \frac{U}{4t} \simeq 2.5 .$$

In fact, several quantum oscillation experiments give consistently an effective quasiparticle mass of carrier in the overdoped region which is approximately twice the effective quasiparticle mass of carriers in the underdoped region.

It is interesting to compare the low-temperature linear term in the electronic specific heat of the quasiholes with the one of the nodal quasidelectrons evaluated in Sect. 4.4. Since the quasiholes behave like a two-dimensional normal Fermi liquid, we obtain instead of Eq. (4.56):

$$(5.2) \quad \gamma_s \simeq \frac{\pi}{3} \frac{m_h^* a_0^2}{\hbar^2} N_A k_B^2 .$$

In fact, it is easy to check that the Sommerfeld coefficient given by Eq. (5.2) exceeds by about an order of magnitude the quasidelectron Sommerfeld coefficient. Using our hole effective mass we obtain (MKS units):

$$(5.3) \quad \gamma_s \simeq 8.53 \text{ mJ mol}^{-1} \text{K}^{-2} .$$

Our determination of γ_s compares quite well with the observed value:

$$(5.4) \quad \gamma_s \simeq 7 \pm 1 \text{ mJ mol}^{-1} \text{K}^{-2}$$

as obtained from direct measurements in polycrystalline $Tl_2Ba_2CuO_{6+\delta}$ [72], independently on δ , and also from indirect determination through the effective hole mass $m_h^* = (5.2 \pm 0.4)m_e$ in Ref. [63].

Concerning the superconducting phase in the overdoped region, we already argued that this can be described within the conventional BCS framework. In fact, there is a large body of evidence that the weak-coupling d-wave BCS approach accounts for many of the low-energy and low-temperature properties of overdoped copper oxides. Here, we restrict ourself to the discussion of a clear signature of d-wave BCS pairing in momentum space, namely the ratio of the BCS gap to the critical temperature anticipated in Eq. (3.61):

$$(5.5) \quad \frac{\Delta_{BCS}}{k_B T_c} \simeq \frac{2\pi}{\sqrt{e}} e^{-\gamma} \simeq 2.14 .$$

To derive Eq. (5.5), we observe that the gap equation Eq. (3.47) at finite temperature reads:

$$(5.6) \quad \Delta(\vec{k}) = -\frac{1}{2} \sum_{\vec{k}'} \frac{V(\vec{k} - \vec{k}') \Delta(\vec{k}')}{\sqrt{\xi_{\vec{k}'}^2 + |\Delta(\vec{k}')|^2}} \tanh \left[\frac{\sqrt{\xi_{\vec{k}'}^2 + |\Delta(\vec{k}')|^2}}{2 k_B T} \right] .$$

Thus, instead of Eq. (3.56) we have:

$$(5.7) \quad 1 \simeq -V_2 \int \frac{d\vec{k}'}{(2\pi)^2} \frac{[\cos(2\theta_{k'})]^2}{\sqrt{\xi_{\vec{k}'}^2 + [\Delta_{BCS} \cos(2\theta_{k'})]^2}} \tanh \left[\frac{\sqrt{\xi_{\vec{k}'}^2 + [\Delta_{BCS} \cos(2\theta_{k'})]^2}}{2 k_B T} \right] .$$

Since the critical temperature is defined by $\Delta_{BCS}(T_c) = 0$, we obtain:

$$(5.8) \quad 1 \simeq -\frac{V_2 m_h^*}{\hbar^2} \int_{-\varepsilon_c}^{+\varepsilon_c} \frac{d\xi}{(2\pi)^2} \int_0^{2\pi} d\theta \frac{[\cos(2\theta)]^2}{|\xi|} \tanh \left[\frac{|\xi|}{2 k_B T_c} \right] ,$$

i.e.

$$(5.9) \quad 1 \simeq -\frac{V_2 m_h^*}{2\pi \hbar^2} \int_0^{\varepsilon_c} \frac{d\xi}{\xi} \tanh \left[\frac{|\xi|}{2 k_B T_c} \right] .$$

Upon using Eq. (3.60) we may rewrite Eq. (5.9) as:

$$(5.10) \quad 1 \simeq \lambda_2 \int_0^{\frac{\varepsilon_c}{2k_B T_c}} \frac{dz}{z} \tanh[z] \simeq \lambda_2 \left[\ln\left(\frac{\varepsilon_c}{2k_B T_c}\right) - \ln\left(\frac{\pi}{4}\right) + \gamma \right] ,$$

which leads to:

$$(5.11) \quad k_B T_c \simeq \frac{\varepsilon_c}{2} \exp\left(-\ln\frac{\pi}{4} + \gamma\right) \exp\left[-\frac{1}{\lambda_2}\right] .$$

Combining Eq. (5.11) with Eq. (3.59) one obtains Eq. (5.5). In Figure 12 we display the doping dependence of the ratio Eq. (5.5) using the data reported in Fig. 4 of Ref. [73]. It is evident that in the overdoped region $\delta \gtrsim 0.20$ the gap values approach closely onto the theoretical prediction of the weak-coupling d-wave BCS superconductivity.

Let us now discuss the optimal doped region $\delta \sim \delta_{opt}$. According to our picture, the low-doping region is characterized by a large pseudogap $\Delta_2(\delta)$ which decreases rapidly

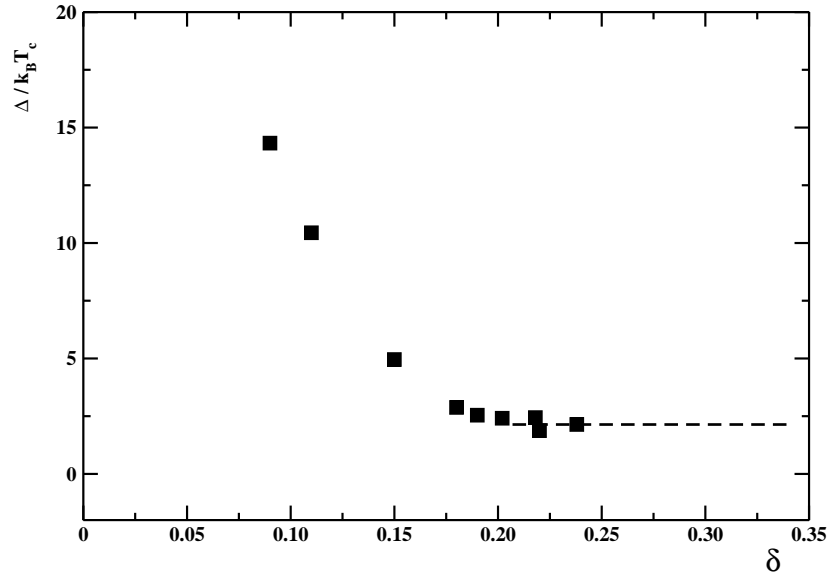


Fig. 12. – Doping dependence of the ratio of superconducting gap Δ over the critical temperature T_c . The data has been extracted from Fig. 4 of Ref. [73]. The dashed line is the weak coupling d-wave BCS value $\frac{\Delta}{k_B T_c} \simeq 2.14$.

with increasing doping, while the superconductivity is driven by the finite-temperature Berezinskii-Kosterlitz-Thouless transition with a critical temperature that increases with doping. On the other hand, in the overdoped region the superconducting transition is well described by the conventional weak-coupling d-wave BCS pairing in momentum space. The decrease of the critical temperature with increasing doping level originates from the underlying reduction in the pairing strength due to the disturbing of the anti-ferromagnetic correlations with overdoping. From our Fig. 7 we see that the two critical temperatures meet in the optimal doped region $\delta \sim \delta_{opt}$, explaining in a natural way why the critical superconducting temperature reaches here the maximum value. Since the Berezinskii-Kosterlitz-Thouless temperature is comparable to the BCS critical temperature, this makes fluctuations much more important. Even more, Fig. 7 suggests that also the pseudogap temperature T^* becomes comparable to both T_{B-K-T} and T_{BCS} . We conclude, thus, that in this region of the phase diagram there are competing phases and it is quite difficult to precisely pin down the underlying physics. On the other hand, as our Fig. 7 is suggesting, there is a large body of evidence that pseudogap energy scale does not extend into the heavily overdoped region of the phase diagram, but rather collapse at a well defined critical concentration around $\delta^* \simeq 0.20$. We would like to stress that the presence of an expanded phase-fluctuation regime in the optimal doped region may explain why certain spectroscopic probes, like angle-resolved photoemissions, tend to advocate scenarios in which the pseudogap temperature tracks the superconducting dome rather than vanishing inside it. The scenario advanced in this paper is supported by the results presented in Ref. [74]. By means of a systematic electronic Raman scattering study of a mercury-based single layer cuprate as a function of doping level, the authors of Ref. [74] revealed the existence of a breakpoint close to optimal doping, below which the

antinodal gap (the pseudogap) is gradually disconnected from superconductivity. The nature of both the superconducting and normal state is distinctly different on each site of this breakpoint. This is consistent also with electronic specific heat measurements. In fact, it turns out that [75, 76] in optimally and overdoped samples the Sommerfeld coefficient is almost constant for $T > T_c$, in accord with our Eq. (5.2), while for underdoped samples there is considerable drop in the Sommerfeld coefficient for $T < T^*$ (see our Eq. (4.56)). Moreover, there is evidence for carrier density which decreases smoothly from $\frac{1+\delta}{a_0^2}$ in the overdoped phase to $\frac{\delta}{a_0^2}$ in the underdoped phase. In fact, in Refs. [77, 78] it is shown that it exists a critical point δ^* where the pseudogap temperature T^* goes to zero and which lies in the superconducting dome. Just below δ^* there is a crossover from a metal with large hole-like Fermi surface, consistent with $n_h \simeq \frac{1+\delta}{a_0^2}$, to a metal with low density of charge carrier, which from Hall and Seebeck effect measurements are quasielectrons, with $n_e \simeq \frac{\delta}{a_0^2}$.

Before concluding this Section, we would like to remark that the optimal doped region of hole-doped cuprates is the most difficult to precisely characterize. In fact, according to our current theoretical understanding, in this region there is competition between the BCS gap and the pseudogap, and the presence of sizable phase fluctuations strongly limit our mean-field treatment. Nevertheless, it is worthwhile to discuss the dependence of the maximum critical temperature T_c^{max} on the microscopic parameters of the model. As already discussed we have:

$$(5.12) \quad T_c^{max} \simeq T_{BCS}(\delta_{opt} \simeq \delta^*).$$

Now, from Eqs. (2.5), (2.9), (2.17), (3.46) and (3.60) we obtain:

$$(5.13) \quad T_c^{max} \sim \frac{t^2}{U} \exp\left[-\frac{1}{(1 - \delta^*/\delta_c)^2}\right]$$

where we recall that δ^* is the hole doping fraction where the pseudogap Δ_2 vanishes. Apparently Eq. (5.13) suggests that one can increase T_c^{max} by increasing $\frac{t^2}{U}$ and/or decreasing δ^* . However, it turns out that the increase of $\frac{t^2}{U}$ leads also to an increase of δ^* and vice versa, such that the two effects compensate in Eq. (5.13). This explains why the optimal hole doping fraction is very close to δ^* and attains the universal value:

$$(5.14) \quad \delta_{opt} \simeq \delta^* \simeq 0.20$$

in the whole family of cuprates.

6. – The electron doped cuprates

The vast majority of high-temperature superconductors are hole-doped. Nevertheless, in this Section we will touch upon high-temperature electron-doped cuprates (see Ref. [19] for a review). The most evident difference between electron and hole doped cuprates is that the antiferromagnetic phase at $\delta = 0$ is much more robust in the electron-doped material and it persists to much higher doping levels. If we adopt the effective single-band Hubbard model of Sect. 1 for the microscopic description of the CuO_2 layers, then we see that the electrons injected into the copper-oxide plane would behave like the holes in the overdoped region of the hole-doped cuprates. However, due to the stronger

antiferromagnetic correlations in the ground state for $\delta > 0$, the electron carrier density is:

$$(6.1) \quad n_e \simeq \frac{\delta}{a_0^2} ,$$

since one electron of the $(1 + \delta)$ electrons per Cu atom is frozen in the half-filled Hubbard band antiferromagnetic configuration. In our approach the effective Hamiltonian for the injected electrons should be given by Eqs. (2.18) and (2.6). In particular, the electron effective mass agrees with Eq. (2.17):

$$(6.2) \quad m_e^* \simeq \frac{\hbar^2}{8 \frac{t^2}{U} a_0^2} \simeq 5.41 m_e$$

with the previously stated values of the model parameters. However, due to the increased role played by the fermion correlations in the antiferromagnetic background, we expect that the effective two-body potential in the interaction Hamiltonian Eq. (2.6) is reduced to some extent. To take into account this effect, we shall assume that the effective potential $V(\vec{r}_1 - \vec{r}_2)$ has the same form as in Eq. (2.7) but with a somewhat reduced interaction length:

$$(6.3) \quad r_0^{(e)}(\delta) = 4.15 a_0 \left(1 - \frac{\delta}{\delta_c}\right)^{\frac{1}{2}} , \quad \delta_c \simeq 0.35 .$$

We now show that this small variation in the range of the effective two-body interaction potential leads to a dramatic change in the phase diagram of the electron-doped cuprates. In fact, by solving the real-space d-wave bound state Schrödinger equation Eq. (3.11) we find a drastically reduced pseudogap (see Fig. 13):

$$(6.4) \quad T_{(e)}^*(\delta = 0) = \frac{\Delta_2^{(e)}(\delta = 0)}{2 k_B} \simeq 46 K , \quad \delta^* \simeq 0.05 .$$

This means that, according to the discussion in Sect. 3.2, the pseudogap superconducting phase of the underdoped region of hole-doped cuprates is absent. Therefore, the superconducting transition in electron-doped cuprates is driven by the weak-coupling d-wave BCS pairing in momentum space. In this case the critical BCS temperature is given by Eq. (3.62):

$$(6.5) \quad k_B T_{BCS}^{(e)}(\delta) \simeq \frac{2e^\gamma}{\pi} \Delta_2^{(e)}(0) \exp\left[-\frac{1}{\lambda_2^{(e)}(\delta)}\right]$$

with $\Delta_2^{(e)}(0)$ given by Eq. (6.4),

$$(6.6) \quad \lambda_2^{(e)} = \frac{m_e^* V_0}{\hbar^2} \int_0^{r_0^{(e)}(\delta)} dr r \left[J_2(k_F^{(e)} r) \right]^2 ,$$

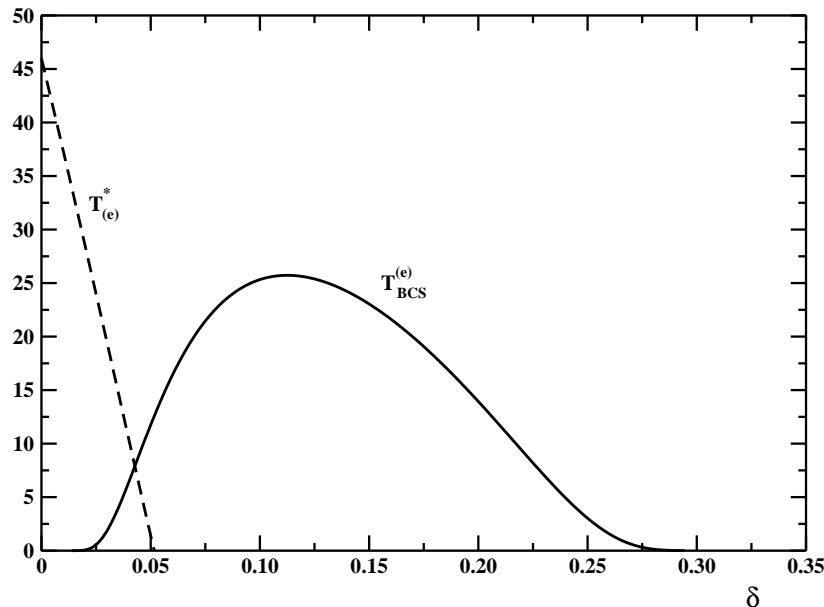


Fig. 13. – The pseudogap and BCS critical temperatures (in Kelvin) versus the doping fraction for the electron-doped cuprates.

and

$$(6.7) \quad k_F^{(e)} \simeq \frac{\sqrt{2\pi\delta}}{a_0} .$$

The BCS critical temperature Eq. (6.5) as a function of the electron doping level is displayed in Fig. 13. From the schematic phase diagram we infer that the maximal critical temperature is strongly reduced with respect to the hole-doped cuprates. Moreover, the superconducting phase manifests itself in a rather narrow interval of doping around $\delta \simeq 0.12$. These general aspects of our phase diagram seem to be in qualitative agreement with observations. However, a thorough understanding of the superconductivity in electron doped cuprates must await more detailed experimental informations.

7. – Summary and Conclusions

The driving principle of the approach presented in this paper has been that the high-temperature superconductivity can be understood within some framework along the line of the microscopic theory of Bardeen, Cooper, and Schrieffer. The results presented in this paper summarize our attempts over the last years to construct a comprehensive model that gives all aspects of the unusual behavior seen in the various regions of the phase diagram of the cuprates. It is obvious that we must rely heavily on some assumptions. First, we assumed that the physics of the high-temperature cuprates is deeply rooted in the copper-oxide planes. This allowed us to completely neglect the motion along the direction perpendicular to the CuO_2 planes. Our second main assumption has been that the single-band effective Hubbard model is sufficient to account for all the

essential physics of the copper-oxide planes. Both assumptions are well accepted and superbly illustrated in the Anderson's book [11]. Accordingly, we have proposed an effective Hamiltonian that is able to govern the dynamics of the electrons or holes injected into the undoped copper-oxide planes. We arrived at our effective Hamiltonian by using arguments well-known in the literature on the motion of charge carriers in an antiferromagnetic background. Notwithstanding, we were unable to offer a truly microscopic derivation of the effective Hamiltonian. So that our arguments to determine the effective Hamiltonian, albeit suggestive, cannot be considered a first principle derivation. In spite of that, we showed that the effective Hamiltonian offers us a consistent picture of the high transition temperature cuprate superconductors. Due to the reduced dimensionality the two-body attractive potential admits real-space d-wave bound states. The binding energy of these bound states, which plays the role of the pseudogap, decreases with increasing doping until it vanishes at a certain critical doping $\delta = \delta^*$. This allows us to reach the conclusion that the key features of the underdoped side of the phase diagram are controlled by very strong pairing that is phase-disordered by thermal fluctuations. We also were able to estimate the upper critical magnetic field whose strength and doping dependence are in good agreement with observations. We obtain a clear explanation for the so-called vortex region and for the puzzling discrete states bounded to the core of isolated vortices. We have discussed how the presence of the pseudogap is responsible for the formation of the quasielectron nodal Fermi liquid which, in turn, leads to the Fermi arcs observed in angle-resolved photoemission studies and to the Fermi pockets in quantum oscillation experiments. We have found a natural explanation for the peculiar dependence of the specific heat on the applied magnetic field observed in underdoped cuprates. However, we would like to stress that we did not attempt a complete discussion of the strange behavior of the cuprates in this region. In particular, as already pointed out in Sect. 4, we did not discuss the so-called nodal gap. In fact, we plan to present in a separate paper a detailed discussion on the origin and temperature dependence of the nodal gap, on the thermal conductivity, on the departure from the Wiedemann-Franz law and on the London penetration depth.

In our model the overdoped region is realized for hole doping in excess of the critical doping δ^* where the pseudogap vanishes. In this region the conventional d-wave BCS framework account for many of the low-energy and low-temperature properties of the copper oxides, in agreement with several observations. Finally, we explain naturally why the superconducting critical temperature reaches its maximum in the optimal doped region. We pointed out that in this region the competition between the pseudogap and the d-wave BCS gap together with the enhanced role of the phase fluctuations makes questionable the usually adopted mean-field approximation. We have also briefly discussed the comparatively less-studied electron-doped cuprates. We suggest that the dome-shaped superconducting region in electron-doped copper-oxides can be described by the conventional weak-coupling d-wave pairing in momentum space.

In conclusion, the fact that a relatively simple model for the effective Hamiltonian allowed to recover several observational features of the high-temperature copper oxides, suggests that the approach presented in this paper could be considered a significative step toward a microscopic explanation of the high-temperature superconductivity in cuprates.

REFERENCES

- [1] J. G. Bednorz and K. A. Müller, *Z. Phys. B* **64** (1986) 189

- [2] A. Damascelli, Z. Hussain and Z. X. Shen, Rev. Mod. Phys. **75** (2003) 473
- [3] G. Deutscher, Rev. Mod. Phys. **77** (2005) 109
- [4] D. N. Besov and T. Timusk, Rev. Mod. Phys. **77** (2005) 721
- [5] P. A. Lee, N. Nagaosa, and X. -G. Wen, Rev. Mod. Phys. **78** (2006) 17
- [6] Ø. Fischer, H. Kugler, I. Maggio-Aprile and C. Berthod, Rev. Mod. Phys. **79** (2007) 353
- [7] P. A. Lee, Rep. Prog. Phys. **71** (2008) 012501
- [8] S. Hüfner, M. A. Hossain, A. Damascelli and G. A. Sarvatzky, Rep. Prog. Phys. **71** (2008) 062501
- [9] S. E. Sebastian, N. Harrison and G. G. Lonzarich, Rep. Prog. Phys. **75** (2012) 102501
- [10] P. W. Anderson, Science **235** (1987) 1196
- [11] P. W. Anderson, *The Theory of Superconductivity in the High- T_c Cuprates*, Princeton University Press, Princeton, New Jersey (1997)
- [12] P. W. Anderson, Phys. Rev. **115** (1959) 2
- [13] D. A. Bonn, Nature Physics **2** (2006) 159
- [14] Ch. Niedermayer *et al.*, Phys. Rev. Lett. **80** (1998) 3843
- [15] S. -W. Cheong *et al.*, Phys. Rev. Lett. **67** (1991) 1791
- [16] T. E. Mason, G. Aeppli and H. A. Mook, Phys. Rev. Lett. **68** (1982) 1414
- [17] A. N. Lavrov, L. P. Kozeeva, M. R. Trunin and V. N. Zverev, Phys. Rev. B **79** (2009) 214523
- [18] J. Bardeen, L. N. Cooper and J. R. Schrieffer, Phys. Rev. **106** (1957) 162; Phys. Rev. **108** (1957) 1175
- [19] N. P. Armitage, P. Fournier and R. L. Greene, Rev. Mod. Phys. **82** (2010) 2421
- [20] A. P. Balachandran, E. Ercolelli, and G. Morandi, *Hubbard Model and Anyon Superconductivity*, World Scientific Publishing Co. Inc. (1990)
- [21] K. Huang and E. Manousakis, Phys. Rev. B **36** (1987) 8302
- [22] J. E. Hirsch, Phys. Rev. Lett. **59** (1987) 228
- [23] S. A. Trugman, Phys. Rev. B **37** (1988) 1597
- [24] E. W. Carlson, V. J. Emery, S. A. Kivelson and D. Orgad, *Concepts in High Temperature Superconductivity*, cond-mat/0206217
- [25] J. R. Schrieffer, X. -G. Wen, and S. -C. Zhang, Phys. Rev. Lett. **60** (1988) 944; Phys. Rev. B **39** (1989) 11663
- [26] L. N. Cooper, Phys. Rev. **104** (1956) 1189
- [27] M. R. Schafroth, Phys. Rev. **100** (1955) 463
- [28] J. M. Blatt and S. T. Butler, Phys. Rev. **100** (1955) 476
- [29] P. W. Anderson, Rev. Mod. Phys. **38** (1966) 298
- [30] A. J. Leggett, *Quantum Liquids*, Oxford University Press, Oxford, UK (2008)
- [31] V. L. Berezinskii, Sov. Phys. JETP **32** (1971) 493; Sov. Phys. JETP **34** (1972) 610
- [32] J. M. Kosterlitz and D. J. Thouless, J. Phys. C **6** (1973) 1181
- [33] B. Vignolle *et al.*, Nature **455** (2008) 952
- [34] P. W. Anderson and P. Morel, Phys. Rev. **123** (1961) 1911
- [35] H. Won and K. Maki, Phys. Rev. B **49** (1994) 1397
- [36] T. Timusk and B. Statt, Rep. Prog. Phys. **62** (1999) 61
- [37] J. L. Tallon and J. W. Loran, Physica C **349** (2001) 53
- [38] U. Chatterjee *et al.*, Nature Physics **6** (2010) 99
- [39] K. Tanaka *et al.*, Science **314** (2006) 1910
- [40] R.-H. He *et al.*, Nature Physics **5** (2009) 119
- [41] A. Pushp *et al.*, Science **324** (2009) 1689
- [42] M. Hashimoto *et al.*, Nature Physics **6** (2010) 414
- [43] T. J. Reber *et al.*, Nature Physics **8** (2012) 606
- [44] S. Sakai *et al.*, *Exploring the Dark Side of Cuprate Superconductors: s-wave Symmetry of the Pseudogap*, arXiv:1207.5070
- [45] T. Yoshida *et al.*, *Coexisting pseudo-gap and superconducting gap in the high- T_c superconductor $La_{2-x}Sr_xCuO_4$* , arXiv:1208.2903
- [46] M. Hashimoto *et al.*, Phys. Rev. B **86** (2012) 094504
- [47] M. Kugler *et al.*, Phys. Rev. Lett. **86** (2001) 4911

- [48] I. Hetel, T. R. Lemberger and M. Randeira, *Nature Physics* **3** (2007) 700
- [49] J. Corson *et al.*, *Nature* **398** (1999) 221
- [50] V. J. Emery and S. A. Kivelson, *Nature* **374** (1985) 434
- [51] M. Tinkham, *Introduction to Superconductivity*, Second Edition, Mc Graw-Hill, Inc., New York (1996)
- [52] Y. Wang, L. Li and N. P. Ong, *Phys. Rev. B* **73** (2006) 024510
- [53] L. Li *et al.*, *Nature Physics* **3** (2007) 311
- [54] J. Chang *et al.*, *Nature Physics* **8** (2012) 751
- [55] Z. A. Xu *et al.*, *Nature* **406** (2000) 486
- [56] C. Capan *et al.*, *Phys. Rev. Lett.* **88** (2002) 056601
- [57] L. Li, Y. Wang, J. G. Checkelsky and M. J. Naughton, *Physica C* **460-462** (2007) 48
- [58] C. Caroli, P. G. de Gennes and J. Matricon, *Phys. Lett.* **9** (1964) 307
- [59] N. Doiron-Leyrand *et al.*, *Nature* **447** (2007) 565
- [60] E. A. Yelland *et al.*, *Phys. Rev. Lett.* **100** (2008) 047003
- [61] A. F. Bangura *et al.*, *Phys. Rev. Lett.* **100** (2008) 047004
- [62] C. Jaudet *et al.*, *Physica B* **404** (2009) 354
- [63] A. F. Bangura *et al.*, *Phys. Rev. B* **82** (2010) 140501
- [64] A. A. Abrikosov, *Introduction to Theory of Normal Metal*, Academic Press, New York and London (1972)
- [65] D. Shoenberg, *Magnetic Oscillations in Metals*, Cambridge University Press, Cambridge (1984)
- [66] D. Le Boeuf *et al.*, *Nature* **450** (2007) 533
- [67] S. Sebastian *et al.*, *Nature Communications* **2** (2011) 471
- [68] F. Laliberte *et al.*, *Nature Communications* **2** (2011) 432
- [69] S. C. Riggs *et al.*, *Nature Physics* **7** (2011) 332
- [70] N. W. Ashcroft and N. D. Mermin, *Solid State Physics*, Harcourt College Publishers (1976)
- [71] G. E. Volovik, *Sov. Phys. JETP* **58** (1993) 469
- [72] J. M. Wade *et al.*, *J. Supercond.* **7** (1994) 261
- [73] Y. Wang *et al.*, *Phys. Rev. B* **76** (2007) 064512
- [74] W. Guyard *et al.*, *Phys. Rev. B* **77** (2008) 024524
- [75] J. W. Loram, K. A. Mirza, J. R. Cooper and J. L. Tallon, *Physica C* **282-287** (1997) 1405
- [76] J. W. Loram, J. Luo, J. R. Cooper and J. L. Tallon, *J. Phys. Chem. Sol.* **62** (2001) 59
- [77] R. Daou *et al.*, *Nature Physics* **5** (2009) 31
- [78] R. Daou *et al.*, *Phys. Rev. B* **79** (2009) 180505